nature metabolism

Article

https://doi.org/10.1038/s42255-024-01176-8

Cellular Feimin enhances exercise performance by suppressing muscle thermogenesis

Received: 27 January 2024

Accepted: 5 November 2024

Published online: 02 January 2025

Check for updates

Ying Peng[1,5], Liangjie Jia[1,5], Xiao Hu[1], Xiaoliu Shi[1], Xinlei Fang[1], Yifu Qiu[2,3], Zhenji Gan[4] & Yiguo Wang[1]

Exercise can rapidly increase core body temperature, and research has indicated that elevated internal body temperature can independently contribute to fatigue during physical activity. However, the precise mechanisms responsible for regulating thermogenesis in muscles during exercise have remained unclear. Here, we demonstrate that cellular Feimin (cFeimin) enhances exercise performance by inhibiting muscle thermogenesis during physical activity. Mechanistically, we found that AMP-activated protein kinase (AMPK) phosphorylates cFeimin and facilitates its translocation into the cell nucleus during exercise. Within the nucleus, cFeimin binds to the forkhead transcription factor FOXC2, leading to the suppressed expression of sarcolipin (*Sln*), which is a key regulator of muscle thermogenesis. In addition, our results further reveal that short-term AMPK agonist treatments can enhance exercise performance through the activation of the AMPK–cFeimin signalling pathway. In summary, these results underscore the crucial role of cFeimin in enhancing exercise performance by modulating SLN-mediated thermogenesis.

Exercise offers a wide range of health benefits and serves as a nonpharmacological approach to prevent and treat chronic metabolic diseases such as obesity, type 2 diabetes and age-related muscle wasting[1–4]. When skeletal muscles contract during exercise, a comprehensive response is triggered, which involves multiple tissues and signalling pathways to meet the heightened energy and oxygen demands[5–10]. Throughout exercise, disruptions in skeletal muscle homoeostasis occur, including changes in PiO_2 levels, alterations in the redox state, increased ATP turnover, higher production of reactive oxygen species and shifts in calcium flux[5–10]. These disturbances activate various sensors, including oxygen sensors such as prolyl hydroxylases, sirtuins, AMP-activated protein kinase (AMPK), mitogen-activated protein kinases and Ca^{2+}/calmodulin-dependent kinase[5–12]. These sensors transmit the exercise-induced signals to downstream transcription factors, which, in turn, activate specific genes related to glucose metabolism, lipid metabolism and mitochondrial biogenesis[5–10,12]. AMPK, functioning as a key exercise sensor that detects changes in the intracellular AMP/ATP ratio, plays a pivotal role in regulating exercise-associated metabolism in skeletal muscle[5,7,10,12–16].

During physical exercise, the production of metabolic heat can increase dramatically, up to 10–20-fold higher than at rest. However, less than 30% of this heat is converted into mechanical energy[8,17]. Dynamic exercise can cause a rapid elevation in core body temperature, and studies have indicated that elevated internal body temperatures can independently contribute to fatigue during exercise[18]. It seems that there may be a threshold temperature at which central fatigue

[1]State Key Laboratory of Membrane Biology, MOE Key Laboratory of Bioinformatics, Tsinghua-Peking Center for Life Sciences, School of Life Sciences, Tsinghua University, Beijing, China. [2]Institute of Molecular Medicine, College of Future Technology, Peking University, Beijing, China. [3]Peking-Tsinghua Center for Life Sciences, Peking University, Beijing, China. [4]State Key Laboratory of Pharmaceutical Biotechnology and MOE Key Laboratory of Model Animal for Disease Study, Model Animal Research Center, Medical School of Nanjing University, Nanjing, China. [5]These authors contributed equally: Ying Peng, Liangjie Jia. e-mail: yiguo@mail.tsinghua.edu.cn

occurs, serving as a protective mechanism to prevent the body from overheating by essentially 'forcing' exercise to cease and avoiding further temperature increase[17,19]. Skeletal muscles are rich in structures such as the sarcoplasmic reticulum (SR) and mitochondria, which play a role in heat generation. The SR is particularly specialized and contains leaky ryanodine receptors (RyR) that increase the activity of SERCA (sarco/endoplasmic reticulum calcium ATPase) pumps. This increased activity results in more ATP hydrolysis and, consequently, more heat production[20,21]. This enhanced heat production is combined with heightened mitochondrial oxidative metabolism to support ATP production and further contribute to heat generation[20,21]. However, uncontrolled release and uptake of calcium ions by the SR can lead to excessive heat production, which is associated with a pathological condition known as 'malignant hyperthermia' (MH). Malignant hyperthermia can occur in pigs and humans due to mutations in the *RYR1* gene[22,23]. These mutations cause excessive calcium leakage from the SR, leading to continuous cycling of the SERCA pump and myosin ATPase, ultimately generating excessive heat[24–26]. Recent research has also highlighted the role of three related SERCA-modulating micropeptides—myoregulin (MRLN), sarcolipin (SLN) and phospholamban (PLN)[27–32]. These micropeptides interact directly with SERCA in the SR membrane to inhibit Ca^{2+} reuptake into the SR to interrupt contraction–relaxation cycles, promote uncoupling of the SERCA pump and induce futile cycling. This futile cycling results in increased ATP hydrolysis and heat production[27–32]. These findings underscore the importance of heat production during exercise for exercise capacity. Nevertheless, the precise mechanisms responsible for regulating thermogenesis in muscles during exercise remain to be fully understood.

In a related study, we discovered a myokine known as Feimin, encoded by *B230219D22Rik* in mice or *C5orf24* in humans, which is induced by feeding and plays a role in regulating glucose homoeostasis. We now show that cellular Feimin (cFeimin) undergoes translocation to the nucleus following phosphorylation by AMPK during exercise. Once in the nucleus, cFeimin interacts with FOXC2, a member of the forkhead transcription factor family, and this interaction leads to the suppression of *Sln* expression, consequently inhibiting muscle thermogenesis. This intriguing signalling cascade ultimately enhances exercise performance. Notably, our findings also suggest that the improved exercise performance observed following short-term treatment with the AMPK agonist AICAR is reliant on the activation of this signalling axis. Therefore, our study sheds light on how exercise-induced signals directly impact thermogenesis, subsequently enhancing exercise performance. Additionally, it highlights the mechanism by which doping with AMPK agonists can enhance physical activity.

Results

Loss of cFeimin in skeletal muscle impairs exercise capacity

To investigate the role of cFeimin in skeletal muscle function, we created mice with a *cFeimin*$^{fl/fl}$ genotype and crossed them with HSA-*Cre* mice to generate muscle-specific *cFeimin* knockout (*cFeimin* MKO) mice. Deficiency of *cFeimin* in skeletal muscle has no discernible effects on body weight, muscle weight, food and water intake, locomotor activity, energy expenditure or grip strength under ad libitum feeding conditions (Extended Data Fig. 1a–g). In addition, when compared with wild-type (WT) (fl/fl) mice, *cFeimin* MKO mice exhibited similar muscle fibre-type compositions in the gastrocnemius (Gas), soleus (Sol) and tibialis anterior muscles (Extended Data Fig. 1h). To explore the significance of cFeimin in exercise performance, we subjected the mice to a maximal exercise capacity test, known as the VO_{2max} test. This test involved gradually increasing the running speed every 2 min on a 5° incline treadmill until exhaustion (Extended Data Fig. 1i). Notably, *cFeimin* MKO mice displayed a significant reduction in maximal speed, total running time and running distance compared with fl/fl mice (Extended Data Fig. 1j–l). Furthermore, *cFeimin* MKO mice exhibited an earlier reaching of maximal VO_2 and respiratory exchange ratio (RER) values during the test, suggesting a quicker onset of fatigue (Extended Data Fig. 1m,n). Collectively, these findings indicate that cFeimin plays a crucial role in enhancing exercise performance during high-intensity exercise challenges.

To further assess the impact of cFeimin on exercise performance and energy utilization, we employed a low-intensity exercise protocol, where mice ran at a constant speed equivalent to 60% of their maximal running speed (Fig. 1a). This protocol was employed for subsequent experiments in our study. In comparison to control littermates, *cFeimin* MKO mice exhibited reduced running time and distance, accompanied by a significant increase in VO_2, VCO_2 and energy expenditure (Fig. 1b–f). The comparable energy substrate utilization as evaluated by RER suggests that *cFeimin* MKO mice expended more energy during exercise (Extended Data Fig. 1o). To further validate this idea, we measured muscle ATP, muscle triglyceride (TG), muscle glycogen and blood glucose levels in fl/fl and *cFeimin* MKO mice before (Sed) and after (Exe) exercise. While muscle ATP and TG levels were similar in sedentary fl/fl and *cFeimin* MKO mice, the *cFeimin* MKO animals displayed significantly lower levels of ATP and TG after exercise (Fig. 1g,h). Additionally, *cFeimin* MKO mice showed reduced muscle glycogen storage and a greater decrease in blood glucose levels after exercise (Fig. 1i,j). All of these results indicate that the absence of *cFeimin* leads to reduced exercise performance but increased energy consumption during physical activity.

cFeimin deficiency promotes *Sln*-mediated heat production

As thermogenesis serves as a primary means of dissipating energy during exercise, we conducted measurements of body temperature in mice during exercise. Notably, although the body temperature of *cFeimin* MKO mice and their control littermates (fl/fl) were comparable at rest (Sed), the body temperature of *cFeimin* MKO mice was significantly higher than that of fl/fl mice during exercise (Fig. 2a,b). To investigate the underlying reasons for the divergent thermogenic responses between fl/fl and *cFeimin* MKO mice, we examined the expression of uncoupling protein 1 (UCP1), a prominent regulator of thermogenesis in brown adipose tissues[33]. Notably, *cFeimin* MKO did not affect the expression of UCP1 at the mRNA and protein levels (Extended Data Fig. 2a,b). Furthermore, *cFeimin* MKO had no discernible impact on the skeletal muscle expression of UCP2 and UCP3, which are important factors in muscle thermogenesis[34] (Extended Data Fig. 2c,d). To investigate whether brown adipose tissue (BAT) thermogenesis regulates exercise and cFeimin, *Ucp1* global KO mice were generated. In comparison with WT, *Ucp1* KO had no discernible effects on exercise performance, body temperature and cFeimin expression in both male and female mice (Extended Data Fig. 2e–h). Together, these data indicate that UCP1-dependent BAT thermogenesis may not significantly regulate the heat production and exercise ability during exercise.

To gain insights into how cFeimin influences thermogenesis, we conducted an investigation into the effect of exercise on gene expression in both fl/fl and *cFeimin* MKO mice. This analysis was performed through RNA sequencing (RNA-seq) on total RNA extracted from the gastrocnemius muscle. The RNA-seq data revealed that following exercise in *cFeimin* MKO mice, 286 genes were upregulated, whereas 46 genes were downregulated in comparison with fl/fl mice (Fig. 2c and Supplementary Table 1). Gene Ontology (GO) analysis showed that the differentially expressed genes were notably enriched in the categories of 'muscle system process' and 'sarcoplasmic reticulum' (Fig. 2d,e and Supplementary Table 2). A heatmap visualization further highlighted the genes enriched in these two categories (Fig. 2f and Supplementary Table 3). Notably, we observed a significant increase in the expression of sarcolipin (*Sln*), a crucial regulator of thermogenesis and metabolism in skeletal muscle[29], in *cFeimin* MKO mice (Fig. 2f and Supplementary Table 3). Accordingly, both

https://doi.org/10.1038/s42255-024-01176-8

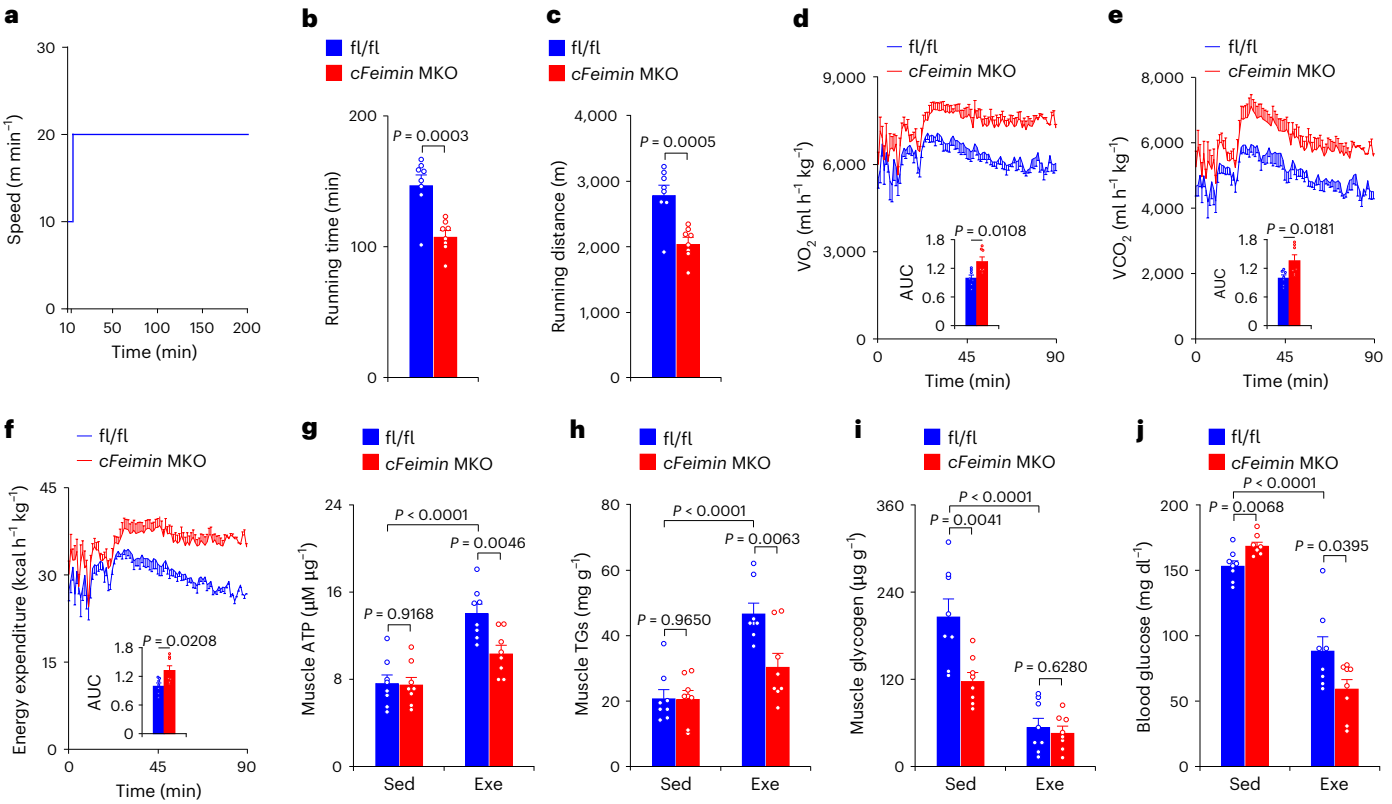

Fig. 1 | Loss of *cFeimin* impairs muscle exercise capacity. a, Schematic showing the speed and duration of treadmill running. **b**,**c**, Running time (**b**) and running distance (**c**) of 10-week-old male WT (fl/fl) and *cFeimin* MKO male mice. $n = 8$ mice. **d**–**f**, VO_2 (**d**), VCO_2 (**e**) and energy expenditure (**f**) of exercising fl/fl and *cFeimin* MKO male mice. $n = 8$ mice. **g**–**j**, Muscle ATP (**g**), muscle TGs (**h**), muscle glycogen (**i**) and blood glucose (**j**) levels in fl/fl and *cFeimin* MKO male mice before (sedentary (Sed)) or after 90 min of exercise (Exe). $n = 8$ mice. Data are shown as mean ± s.e.m. Statistical comparisons were performed using an unpaired two-tailed Student's *t*-test (**b**–**f**) or two-way analysis of variance (ANOVA) followed by Tukey's test (**g**–**j**). All individual points and *P* values are shown.

mRNA and protein levels of *Sln* were found to be elevated in *cFeimin* MKO mice and myotubes (Fig. 2g–i). Consistent with these results, reduced exercise capacity, elevated SLN expression and increased muscle thermogenesis were also observed in female *cFeimin* MKO mice (Extended Data Fig. 3).

Sarcolipin's role in binding to SERCA and blocking Ca^{2+} re-entry from the cytoplasm to the SR results in higher cytosolic Ca^{2+} levels, facilitating uptake of Ca^{2+} into mitochondria to trigger oxidative metabolism[29,35]. Therefore, we measured cytosolic Ca^{2+} levels and oxidative phosphorylation (OXPHOS) in WT and *cFeimin* KO myotubes. Caffeine, an agonist of RYR1, induced a weaker but more sustained cytosolic increase in cytosolic Ca^{2+} levels in *cFeimin* KO myotubes (Fig. 2j). Furthermore, the deficiency of *cFeimin* led to a significant increase in OXPHOS, as evidenced by the higher oxygen consumption rate (OCR) (Fig. 2k). These findings align with the effects observed when sarcolipin is overexpressed[35,36], and suggest that *cFeimin* deficiency affects Ca^{2+} dynamics and OCR in a manner consistent with sarcolipin's role.

To determine whether cFeimin regulates exercise through SLN, we employed short hairpin RNA (shRNA) to suppress *Sln* expression in WT and *cFeimin* MKO mice. The knockdown of *Sln* effectively restored the impact of *cFeimin* MKO on exercise capacity, body temperature and SLN expression in both male and female mice without affecting body weight and muscle glycogen levels (Fig. 3a–g and Extended Data Fig. 3). These data indicate that cFeimin regulates muscle thermogenesis and exercise capacity in an SLN-dependent manner. In addition, the knockdown of *Sln* effectively restored the impact of *cFeimin* KO on calcium dynamics and OCR in the differentiated myotubes (Fig. 3h–j). Taken together, these results indicate that cFeimin suppresses muscle thermogenesis during exercise by inhibiting *Sln* expression.

cFeimin interacts with FOXC2 and suppresses *Sln* expression

As cFeimin suppresses *Sln* expression, we tested its cellular localization and expression during exercise. In skeletal muscle, we observed a slight decrease of cFeimin levels during exercise, accompanied by a clear shift of cFeimin into the nucleus (Fig. 4a). These results indicate that exercise promotes the nuclear translocation of cFeimin. In fact, cFeimin possesses a conserved nuclear localization signal (NLS) (Extended Data Fig. 4). Overexpressed WT cFeimin localizes in both the nucleus and cytoplasm, whereas the NLS-deleted mutant of cFeimin (ΔNLS) is confined to the cytoplasm (Fig. 4b). Notably, the cFeimin ΔNLS mutant is incapable of suppressing *Sln* expression (Fig. 4b). These results collectively suggest that cFeimin relocates to the nucleus during exercise and subsequently reduces *Sln* expression.

To delve into how cFeimin regulates *Sln* expression, we conducted immunoprecipitation experiments followed by mass spectrometry analysis to identify cFeimin's binding proteins. This analysis revealed the transcription factor forkhead box C2 (FOXC2) as a potential binding partner of cFeimin (Fig. 4c and Supplementary Table 4). Co-immunoprecipitation assays confirmed the interaction between cFeimin and FOXC2, with a specific region (amino acids 116–146) of cFeimin being necessary for cFeimin–FOXC2 association (Fig. 4d). Further characterization by amino acid mutation analysis highlighted the significance of Arg124 and Arg140, two conserved amino acids, in the cFeimin–FOXC2 association, as the interaction was abolished when we used the R/D mutant (R124D and R140D) (Fig. 4e).

To examine whether FOXC2 directly regulates *Sln* transcription, we performed chromatin immunoprecipitation (ChIP) assays in myotubes. These assays revealed a strong binding of FOXC2 to the region from −449 to −199 bp upstream of the *Sln* transcription start point (Fig. 4f),

https://doi.org/10.1038/s42255-024-01176-8

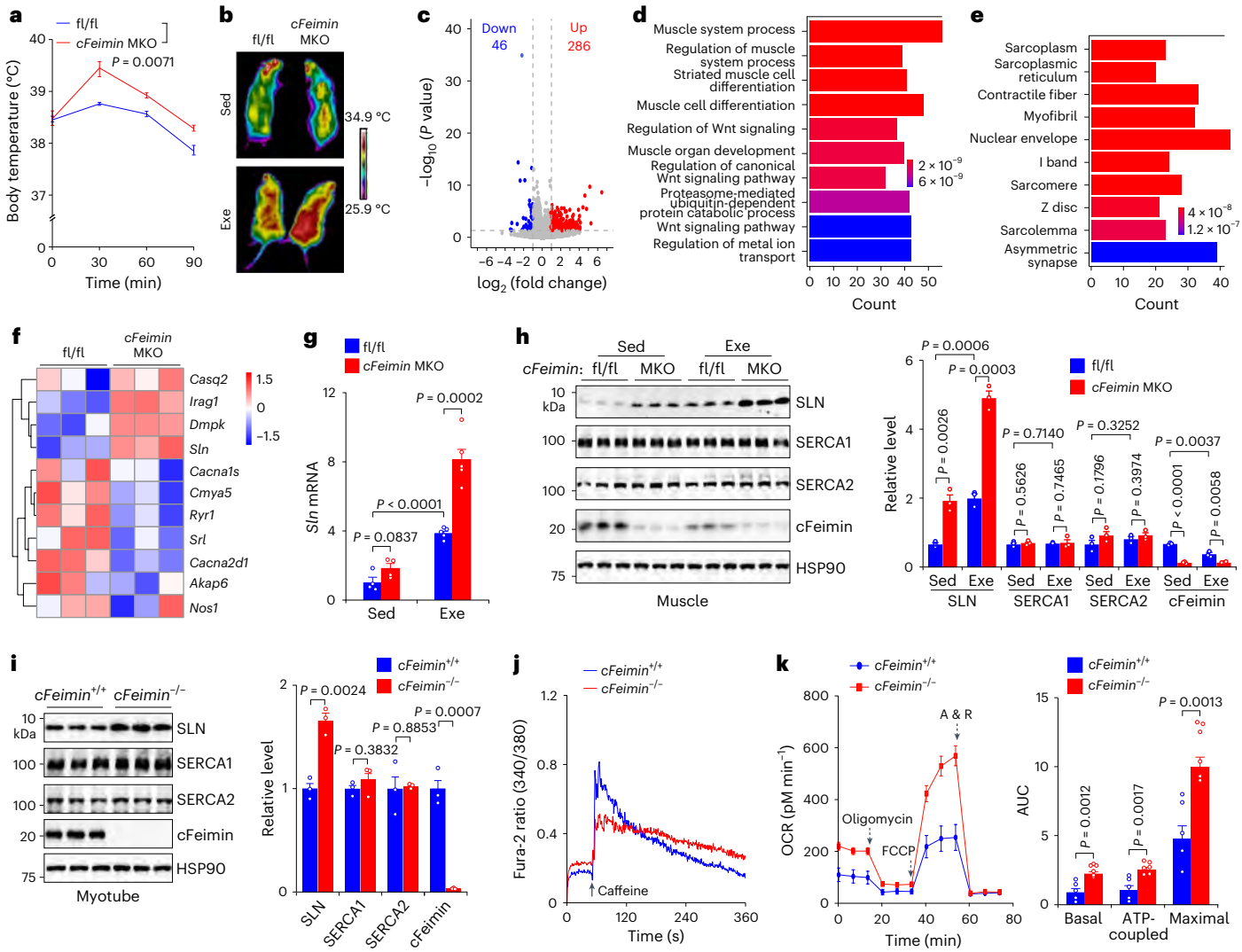

Fig. 2 | *cFeimin* deficiency increases heat production. a,**b**, Rectal temperature (**a**) and body surface temperature (**b**) of 10-week-old male fl/fl and *cFeimin* MKO mice were monitored during exercise. $n = 10$ mice. **c**–**f**, Analysis of exercise-induced changes in gene expression (**c**), GO enrichment analysis was then conducted (**d**,**e**), and a heatmap displaying the gene expression profiles of sedentary and exercised fl/fl and *cFeimin* MKO male mice was generated (**f**). The gastrocnemius muscles of sedentary and exercised (for 90 min) fl/fl and *cFeimin* MKO male mice were collected for total RNA extraction and RNA-seq analysis was performed. **g**,**h**, qPCR (**g**), immunoblotting and statistical data (**h**) showing SLN expression in gastrocnemius muscle extracts from fl/fl and *cFeimin* MKO male mice under sedentary conditions (Sed) or after 90 min of exercise (Exe). $n = 4$ mice (Sed, **g**) and $n = 5$ mice (Exe, **g**), $n = 3$ biological replicates (**h**). **i**–**k**, Immunoblotting (**i**), Ca^{2+} imaging (**j**) and measurement of OCR (left, **k**) were performed and statistical analyses were conducted for immunoblot band intensities (right, **i**), baseline respiratory capacity, ATP-coupled respiratory capacity and maximum respiratory capacity (right, **k**) in differentiated myotubes derived from both WT (*cFeimin*$^{+/+}$) and *cFeimin* global KO (*cFeimin*$^{-/-}$) mice. $n = 3$ biological replicates (**i**), $n = 29$ cells (*cFeimin*$^{+/+}$) and 25 cells (*cFeimin*$^{-/-}$) (**j**), $n = 5$ (*cFeimin*$^{+/+}$) and $n = 6$ biological replicates (*cFeimin*$^{-/-}$) (**k**). Data are shown as mean ± s.e.m. Statistical comparisons were performed using two-way ANOVA followed by Tukey's test (**a**,**g**,**h**) or unpaired two-tailed Student's *t*-test (**i**,**k**). All individual points and *P* values are shown.

indicating the presence of FOXC2-binding motifs in this region. Motif analysis identified three potential FOXC2-binding motifs spanning from −372 to −264 bp of the *Sln* promoter (Fig. 4g). To validate this, we generated myoblasts with a deletion of the region from −384 to −186 bp of the *Sln* promoter. This deletion significantly reduced FOXC2 occupancy and *Sln* expression (Fig. 4g). Together, these results indicate that FOXC2, as a transcription factor, promotes *Sln* expression.

To ascertain whether cFeimin suppresses *Sln* expression via cFeimin–FOXC2 association, we examined the effect of the binding-defective mutant of cFeimin (R/D) on FOXC2 occupancy and *Sln* expression. While *cFeimin* deficiency increased FOXC2 occupancy on the *Sln* promoter and *Sln* expression, the addition of WT cFeimin, but not the R/D mutant of cFeimin, markedly decreased FOXC2 occupancy on the *Sln* promoter and *Sln* expression (Fig. 4h,i). These results are consistent with the data on calcium dynamics and OCR, further confirming that cFeimin promotes calcium influx from the cytoplasm to the SR and inhibits OCR through its interaction with FOXC2 (Fig. 4j,k). Together, these data indicate that cFeimin suppresses *Sln* expression through its binding to FOXC2.

Knockout of *Foxc2* enhances exercise performance

To investigate whether FOXC2 regulates exercise performance, we generated muscle-specific *Foxc2* knockout (MKO) mice. Of note, *Foxc2* MKO mice exhibited comparable body weight, muscle weight, food and water intake, locomotor activity, energy expenditure, grip strength and muscle fibre-type composition under ad libitum feeding conditions when compared with control littermates (Extended Data Fig. 5a–h). In contrast with *cFeimin* deficiency, *Foxc2* MKO male mice demonstrated

https://doi.org/10.1038/s42255-024-01176-8

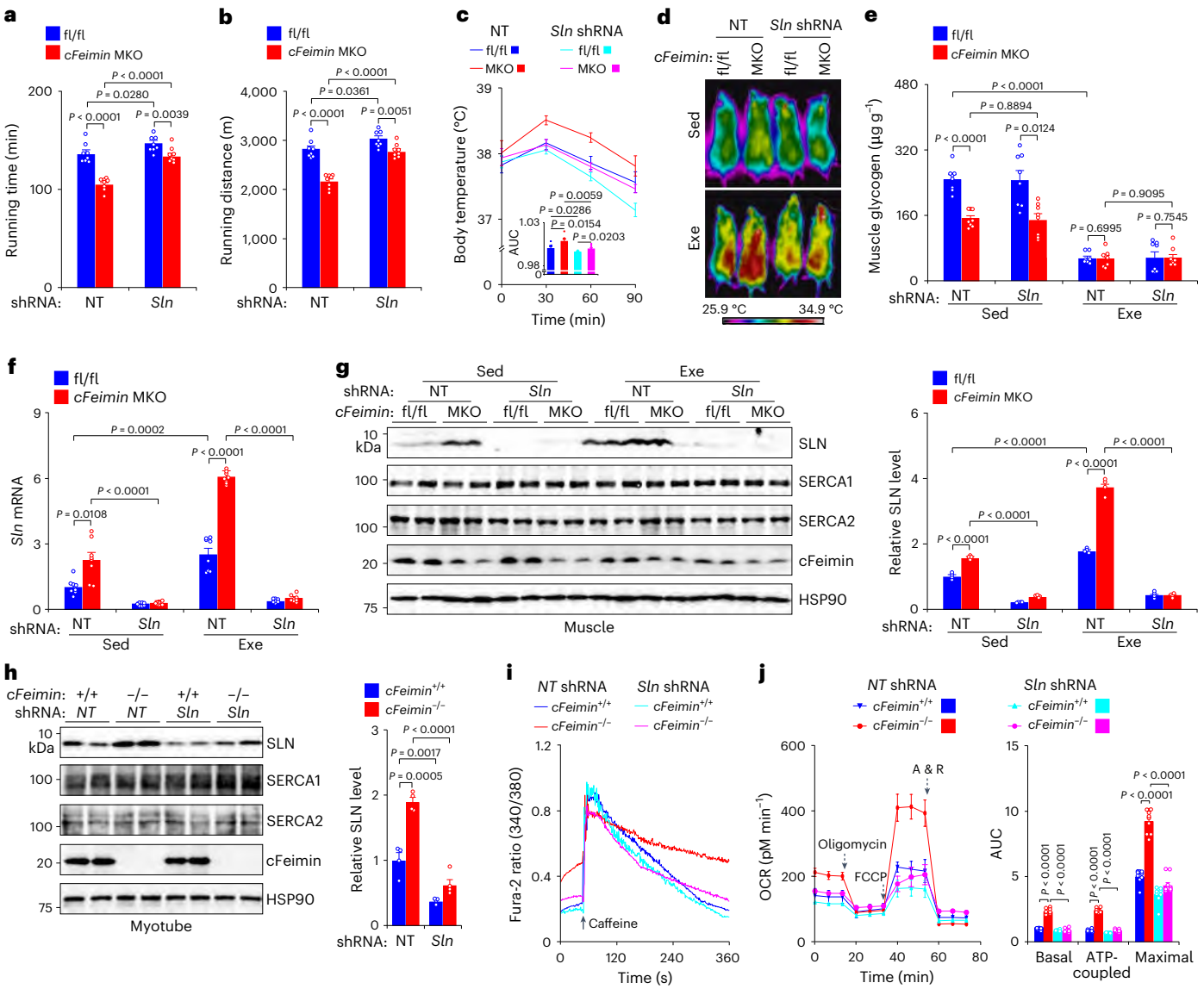

Fig. 3 | cFeimin regulates exercise capacity through SLN. a,**b**, Running time (**a**) and running distance (**b**) of 10-week-old male WT (fl/fl) and *cFeimin* MKO mice with or without *Sln* knockdown by shRNA. $n = 8$ mice. NT, non-targeting shRNA. **c**,**d**, Rectal temperature (**c**) and body surface temperature (**d**) were monitored during exercise in 10-week-old male fl/fl and *cFeimin* MKO mice with or without *Sln* shRNA knockdown. $n = 8$ mice (**c**). **e**, Muscle glycogen levels in 10-week-old male fl/fl and *cFeimin* MKO mice with or without *Sln* shRNA knockdown before (sedentary (Sed)) or after 90 min of exercise (Exe). $n = 8$ mice. **f**,**g**, qPCR (**f**) and immunoblotting and statistical data (**g**) showing SLN expression in gastrocnemius muscle extracts from male mice under sedentary conditions (Sed) or after 90 min of exercise (Exe). $n = 8$ mice (**f**), $n = 4$ biological replicates (**g**). **h**–**j**, Effect of *Sln* knockdown on SLN expression (left, **h**), intracellular Ca^{2+} levels (**i**) and OCR (left, **j**) was assessed, and statistical analyses were carried out for immunoblot band intensities (right, **h**), baseline respiratory capacity, ATP-coupled respiratory capacity and maximum respiratory capacity (right, **j**) in WT (*cFeimin*$^{+/+}$) and *cFeimin* KO (*cFeimin*$^{-/-}$) myotubes. $n = 4$ biological replicates (**h**), $n = 38$ cells (*NT* shRNA, *cFeimin*$^{+/+}$, **i**), $n = 36$ cells (*NT* shRNA, *cFeimin*$^{-/-}$, **i**), $n = 40$ cells (*Sln* shRNA, *cFeimin*$^{+/+}$, **i**), $n = 49$ cells (*Sln* shRNA, *cFeimin*$^{-/-}$, **i**), $n = 10$ biological replicates (**j**). Data are shown as mean ± s.e.m. Statistical comparisons were performed using two-way ANOVA followed by Tukey's test (**a**–**c**,**e**–**h**,**j**). All individual points and *P* values are shown.

an enhancement in exercise capacity, as indicated by increased total running time and distance (Fig. 5a,b). Additionally, compared with control littermates, *Foxc2* MKO male mice displayed decreased VO_2, VCO_2 and energy expenditure (Fig. 5c–e), and higher levels of muscle ATP, muscle TGs, muscle glycogen and blood glucose after exercise (Fig. 5f–i). Consistent with these results, increased exercise capacity was observed in female mice (Extended Data Fig. 5i–k). These findings collectively suggest that *Foxc2* deficiency improves exercise performance while reducing energy consumption.

Although the body temperature of *Foxc2* MKO mice and their control littermates (fl/fl) was comparable at rest, the body temperature of *Foxc2* MKO mice was significantly lower than that of fl/fl mice during exercise in both male and female (Fig. 5j,k and Extended Data Fig. 5l). This is consistent with the observation that *Foxc2* deficiency decreased *Sln* expression in skeletal muscle and myotubes, accelerated calcium influx from the cytoplasm to the SR and attenuated OCR in myotubes (Fig. 5l–p and Extended Data Fig. 5m,n). *Foxc2* MKO had no discernible impact on the expression of UCP1 in BAT and the expression of UCP2 and UCP3 in skeletal muscle (Extended Data Fig. 5o–r). Together, these results indicate that *Foxc2* deficiency in skeletal muscle dampens heat production and enhances exercise capacity, in contrast to the effects of *cFeimin* deficiency.

AMPK drives cFeimin shuttling and lowers *Sln* expression

Previous research has established that AMPK is activated in muscle during exercise and plays a central role in regulating exercise

metabolism[5,7,10,12–16]. Given our observation that exercise promotes cFeimin nuclear translocation (Fig. 4a), we sought to investigate whether AMPK is involved in the nuclear translocation of cFeimin during exercise. To explore this, we injected Compound C, an inhibitor of AMPK, into the gastrocnemius muscle of C57BL/6 male and female mice (the same background as our genetically modified mice) and then subjected them to 90-min exercise after 24 h. Remarkably, Compound C treatment completely blocked the exercise-induced nuclear translocation of cFeimin (Fig. 6a and Extended Data Fig. 6a). To investigate whether AMPK directly phosphorylates cFeimin, we treated myotubes with A769662, an AMPK activator. We then purified cFeimin through immunoprecipitation and identified the phosphorylation sites via mass spectrometry analysis. We identified one conserved phosphorylation site (T128) on cFeimin (Fig. 6b,c). Based on motif scanning of AMPK substrates[37] and conservation analysis of cFeimin, T112 of cFeimin also emerged as a potential phosphorylation site (Fig. 6c). In vitro kinase assays validated that AMPK directly phosphorylates cFeimin at T112 and T128, as the T/A mutant (T112A and T128A) of cFeimin lost the ability to be phosphorylated (Fig. 6d).

To confirm the in vivo phosphorylation of cFeimin, we generated a polyclonal antibody against phospho-cFeimin (pcFeimin) and found that exercise stimulated cFeimin phosphorylation in an AMPK-dependent manner (Fig. 6e and Extended Data Fig. 6b). To determine whether the phosphorylation of cFeimin affects its nuclear translocation, we tested the phosphorylation-defective mutant described above (T/A, T112A and T128A) and a newly generated phosphorylation-mimic mutant (T/D, T112D and T128D). In contrast with WT cFeimin, the T/A mutant of cFeimin was localized in the cytoplasm, whereas the T/D mutant of cFeimin was localized in the nucleus (Fig. 6f). Moreover, neither mutant responded to Compound C treatment in HEK293T cells (Fig. 6f). To investigate the cellular localization of cFeimin mutants in vivo, we expressed cFeimin WT, T/A and T/D in the gastrocnemius muscle of C57BL/6 mice using AAV9-mediated delivery. Exercise promoted the nuclear translocation of WT cFeimin, but not the T/A mutant, whereas the T/D mutant remained constitutively in the nucleus (Fig. 6g and Extended Data Fig. 6c). Consistent with these results, Compound C treatment reduced the nuclear translocation of WT cFeimin (Fig. 6g and Extended Data Fig. 6c). The nucleus-localized T/D mutant, but not the cytoplasm-localized T/A mutant of cFeimin, was able to restore the inhibitory effects of cFeimin on FOXC2 occupancy on the *Sln* promoter and *Sln* expression (Fig. 6h,i). T/D, but not T/A, also restored calcium re-entry into the SR and reduced the OCR (Fig. 6j,k). Overall, these data demonstrate that AMPK phosphorylates cFeimin, promotes its nuclear translocation and, thereby, reduces *Sln* expression.

cFeimin suppresses *Sln* expression by binding to FOXC2

To investigate whether nucleus-localized cFeimin suppresses *Sln* expression in vivo by binding to FOXC2, we administered injections of AAV9-mediated WT cFeimin, as well as the T/A, T/D and R/D mutants of cFeimin, into the gastrocnemius muscle of cFeimin MKO mice. *cFeimin* MKO dramatically increased exercise-induced *Sln* expression, whereas the addition of WT cFeimin or the nucleus-localized T/D mutant, but not the cytoplasm-localized T/A mutant or the FOXC2-binding-defective mutant (R/D), led to a significant reduction in *Sln* expression (Fig. 7a,b). These results underscore the necessity of the cFeimin–FOXC2 interaction for the inhibitory effect of cFeimin on *Sln* expression in the skeletal muscle.

To validate whether FOXC2 acts as a mediator of cFeimin's inhibitory role in *Sln* expression, we assessed the impact of cFeimin overexpression and knockdown in *Foxc2* MKO mice. Muscle knockout of *Foxc2* decreased *Sln* expression, and notably, cFeimin overexpression did not further affect *Sln* expression (Fig. 7c,d). Conversely, akin to *cFeimin* MKO, *cFeimin* knockdown increased *Sln* expression, but this effect was nearly abolished in *Foxc2* MKO mice (Fig. 7e,f). These collective findings strongly suggest that exercise promotes the nuclear translocation of cFeimin and its inhibitory influence on *Sln* expression through the cFeimin–FOXC2 association in skeletal muscle.

AMPK promotes exercise performance via cFeimin and FOXC2

To determine whether AMPK regulates exercise performance via affecting muscle thermogenesis, we generated skeletal muscle-specific AMPKα1/AMPKα2 knockout (*Ampk* MKO) mice. *Ampk* MKO mice showed significantly decreased exercise performance and sedentary glycogen levels (Fig. 8a–c), which is consistent with previous studies[38–42]. Although the body temperature of *Ampk* MKO mice and WT was comparable at rest, the body temperature of *Ampk* MKO mice was significantly higher than that of WT mice during exercise (Fig. 8d,e). Accordingly, both mRNA and protein levels of Sln were increased in *Ampk* MKO mice (Fig. 8f,g). These data indicate that *Ampk* MKO mice show a similar phenotype to *cFeimin* MKO mice during exercise.

Doping refers to the use of drugs that enhance cellular fat-burning abilities and improve exercise endurance. Several AMPK activators, such as AICAR, GW1516, SR9009 and trimetazidine, have been listed as doping agents in the World Anti-Doping Code published by the World Anti-Doping Agency[43–45]. As AMPK promotes the inhibitory role of cFeimin in *Sln* expression through the cFeimin–FOXC2 association, we aimed to investigate whether cFeimin and FOXC2 mediate the enhancement of exercise performance by AMPK-related doping agents. To identify the most effective AMPK activator among these doping agents, we treated myotubes with AICAR, GW1516, SR9009 and trimetazidine. Subsequently, we assessed AMPK activation and *Sln* expression. Our findings revealed that AICAR is the most potent AMPK activator and significantly suppresses *Sln* expression in myotubes (Extended Data Fig. 7a,b). Based on these results, we chose AICAR to explore the roles of cFeimin and FOXC2 in enhancing exercise performance.

Fig. 4 | cFeimin binds to FOXC2 and suppresses *Sln* expression. **a**, Immunostaining (left) and statistical data (top right) showing nuclear translocation of cFeimin and protein levels (bottom right) in the gastrocnemius muscle at various exercise (Exe) times. $n = 6$ male mice. DAPI, 4,6-diamidino-2-phenylindole. **b**, Localization of WT cFeimin and cFeimin ΔNLS, with a deletion of the NLS, in differentiated myotubes (top). The effects of WT cFeimin and the ΔNLS mutant of cFeimin on *Sln* mRNA expression in myotubes (bottom). $n = 4$ biological replicates. **c**, Silver-stained gel showing the proteins interacting with cFeimin in myotubes (left) and the peptides of FOXC2 identified through mass spectrometry analysis (right). The red boxes highlight the bands that were excised for mass spectrometry analysis. Specifically, FOXC2 was identified from band 1. **d**, Deletion analysis of the regions in cFeimin required for the cFeimin–FOXC2 interaction is presented (top). Interaction-competent FOXC2 is indicated by (+) in each schematic. Co-immunoprecipitation (co-IP) shows the interaction of FOXC2 with WT cFeimin or its mutants (bottom). **e**, The location of two highly conserved Arg (R) residues within the FOXC2-binding region of cFeimin (top). These two residues were mutated to Asp (D) to create the R/D mutant of cFeimin. Co-IP demonstrates the interaction between FOXC2 and WT or R/D cFeimin. **f**, ChIP–qPCR showing the FOXC2-binding region within the *Sln* promoter. $n = 3$ biological replicates. **g**, FOXC2-binding motif and predicted binding sites within the *Sln* promoter (left). The effect of the WT *Sln* promoter and the deleted *Sln* promoter (with predicted FOXC2-binding sites removed) on FOXC2 occupancy (middle). The effect on *Sln* expression (right). $n = 4$ biological replicates. **h**–**k**, The impact of WT or R/D cFeimin on FOXC2-binding capacity within the *Sln* promoter (**h**), *Sln* expression (**i**), cellular Ca^{2+} levels (**j**) and OCR (**k**) in *cFeimin* WT (*cFeimin*$^{+/+}$) and KO (*cFeimin*$^{-/-}$) myotubes. $n = 4$ biological replicates (**h**,**i**), $n = 18$ cells (*cFeimin*$^{+/+}$,**j**), $n = 17$ cells (*cFeimin*$^{-/-}$,**j**), $n = 20$ cells (*cFeimin*$^{-/-}$ + WT,**j**), $n = 23$ cells (*cFeimin*$^{-/-}$ + R/D,**j**), $n = 5$ biological replicates (*cFeimin*$^{+/+}$, **k**), $n = 7$ biological replicates (*cFeimin*$^{-/-}$, **k**), $n = 6$ biological replicates (*cFeimin*$^{-/-}$ + WT, **k**), $n = 8$ biological replicates (*cFeimin*$^{-/-}$ + R/D, **k**). Data are shown as mean ± s.e.m. Statistical comparisons were performed using two-way ANOVA followed by Tukey's test (**a**,**b**,**g**–**i**,**k**) or unpaired two-tailed Student's *t*-test (**f**). All individual points and *P* values are shown.

https://doi.org/10.1038/s42255-024-01176-8

To eliminate potential confounding effects on muscle development and fibre reprogramming, we subjected mice to short-term AICAR treatment (daily injection for 2 weeks). As illustrated in Extended Data Fig. 7c–p, AICAR treatment did not affect the expression of genes related to myogenesis and myofiber types. Nevertheless, AICAR treatment led to a decrease in *Sln* expression, a reduction in body temperature, an increase in muscle glycogen levels and an increase in total running time and distance in WT (fl/fl) mice (Fig. 8h–n). Notably, *cFeimin* MKO mice did not exhibit the same improvements in exercise performance upon AICAR treatment (Fig. 8h–n). Moreover, no additional benefits of AICAR were observed in *Foxc2* MKO mice (Fig. 8h–n). Taken together, our findings demonstrate that cFeimin and FOXC2 mediate the enhancement of exercise performance induced by AICAR.

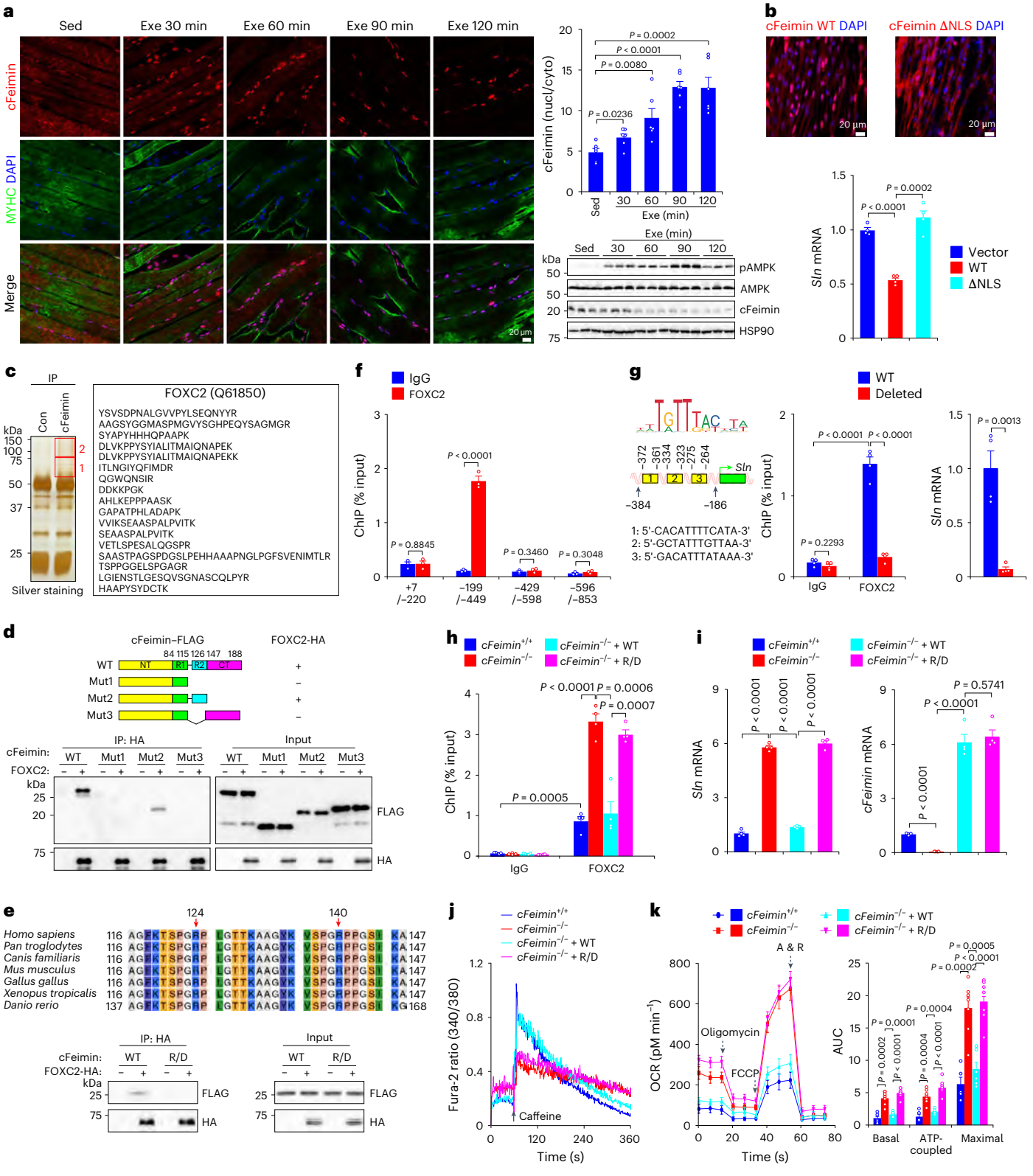

https://doi.org/10.1038/s42255-024-01176-8

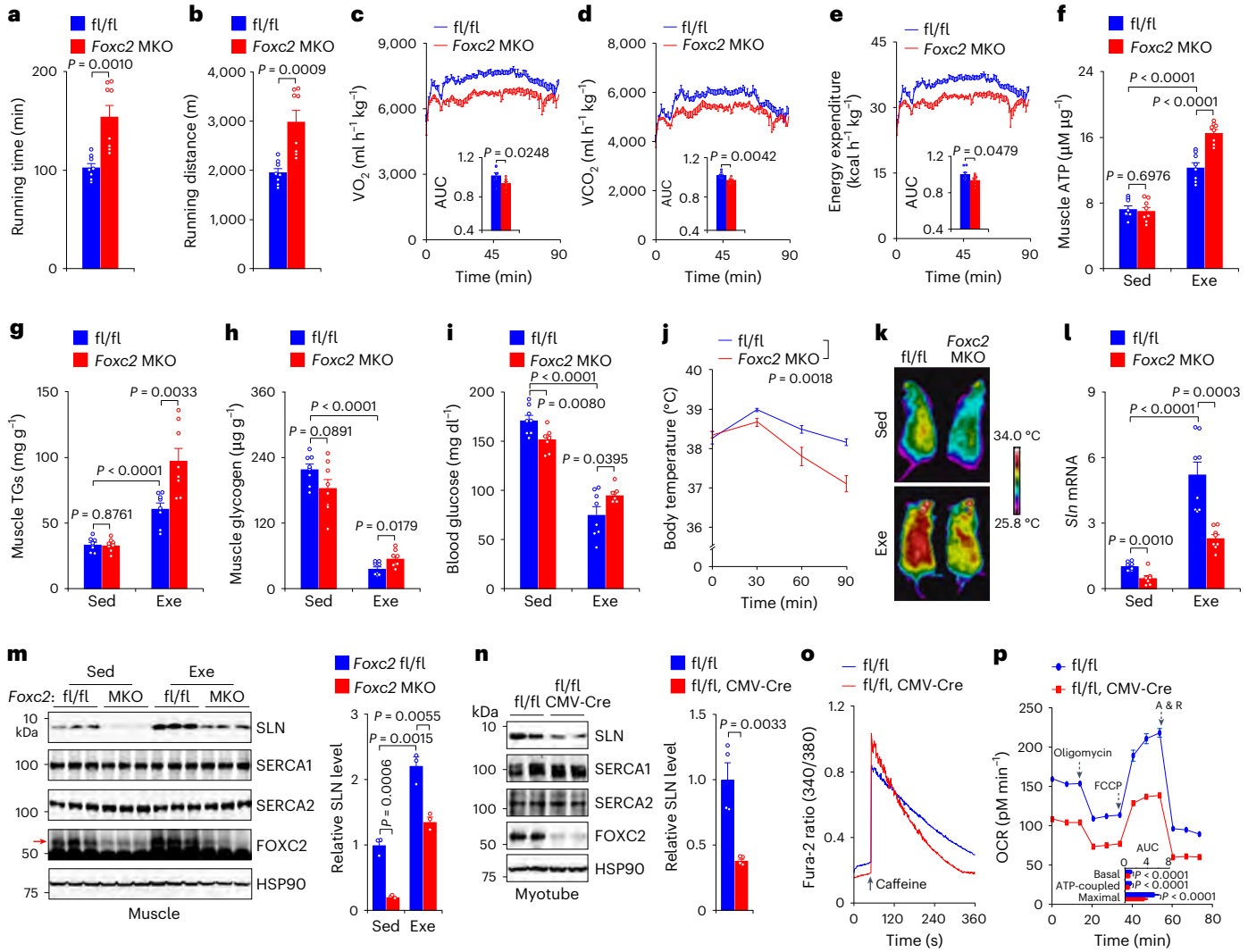

Fig. 5 | Knockout of *Foxc2* enhances muscle exercise capacity. a,**b**, Running time (**a**) and running distance (**b**) were measured in 10-week-old male fl/fl and *Foxc2* muscle-specific knockout (MKO) mice. $n = 8$ mice. **c**–**e**, VO_2 (**c**), VCO_2 (**d**) and energy expenditure (**e**) were assessed in exercising male fl/fl and *Foxc2* MKO mice. $n = 8$ mice. **f**–**i**, Levels of muscle ATP (**f**), muscle TGs (**g**), muscle glycogen (**h**) and blood glucose (**i**) were determined in male fl/fl and *Foxc2* MKO mice under sedentary (Sed) conditions and after 90 min of exercise (Exe). $n = 8$ mice. **j**,**k**, Rectal temperature (**j**) and body surface temperature (**k**) were recorded for male fl/fl and *Foxc2* MKO during exercise. $n = 10$ mice (**j**). **l**,**m**, qPCR (**l**) and immunoblots and statistical data (**m**) showing SLN expression in gastrocnemius muscle extracts from male fl/fl and *Foxc2* MKO mice under sedentary (Sed) conditions and after 90 min of exercise (Exe). On the immunoblot, FOXC2 is denoted by the red arrow. $n = 8$ mice (**l**), $n = 3$ biological replicates (**m**). **n**–**p**, The effect of *Foxc2* knockout on SLN protein expression by immunoblotting (**n**; right shows statistical data), cellular Ca^{2+} levels (**o**) and OCR and statistical analyses of baseline respiratory capacity, ATP-coupled respiratory capacity and maximum respiratory capacity (**p**) in differentiated myotubes. B, basal; A, ATP-coupled; M, maximal. $n = 4$ biological replicates (**n**), $n = 28$ cells (fl/fl) and $n = 26$ cells (fl/fl, CMV-Cre) (**o**), $n = 10$ biological replicates (**p**). Data are shown as mean ± s.e.m. Statistical comparisons were performed using an unpaired two-tailed Student's *t*-test (**a**–**e**,**n**,**p**) or two-way ANOVA followed by Tukey's test (**f**–**j**,**l**,**m**). All individual points and *P* values are shown.

Discussion

Exercise can rapidly elevate core body temperature, and studies have indicated that elevated internal body temperature seems to be an independent factor contributing to fatigue during physical activity. However, the mechanisms governing thermogenesis in muscle during exercise have remained unclear. Our findings demonstrate that AMPK activation during exercise phosphorylates cFeimin and facilitates its nuclear translocation. Once in the nucleus, cFeimin binds to FOXC2, leading to the inhibition of *Sln* transcription. This, in turn, promotes Ca^{2+} reuptake into the SR, reduces heat production and enhances exercise performance. Conversely, KO of *cFeimin* leads to an increase in FOXC2-mediated *Sln* expression and heat production, ultimately resulting in a decrease in exercise performance (Fig. 7g). Together, our findings reveal that the AMPK–cFeimin–FOXC2–SLN axis plays a role in muscle exercise, at least in part via SLN-mediated muscle thermogenesis. This is further evidenced by the improved exercise performance observed following AMPK activation by the AMPK agonist AICAR.

Sarcolipin (SLN), myoregulin (MRLN) and phospholamban (PLN) are related micropeptides that modulate SERCA to regulate calcium pump activity in the SR membrane[27–32]. In our RNA-seq data, we observed a significant increase in *Sln* expression in *cFeimin* MKO mice, whereas *Mrln* and *Pln* levels remained unaffected (Supplementary Table 1). This suggests that *Mrln* and *Pln* do not play a significant role in cFeimin's function in skeletal muscle. In skeletal muscle, SLN overexpression reduces both peak twitch force and tetanic force, as well as the rates of contraction and relaxation[46]. Loss of *Sln* enhances calcium transport and muscle relaxation but does not affect fibre-type switching[47]. Studies from Periasamy's laboratory indicate that skeletal muscle-specific overexpression of SLN leads to increased resistance

to fatigue, significantly longer running distances, reprogramming of mitochondria and enhanced fatty acid oxidation under basal conditions[35,48]. Their research shows that under both pair-feeding (fixed calorie intake) and high-fat-diet conditions (ad libitum feeding), SLN overexpression results in a higher energy cost for muscle work, increased oxidative capacity of skeletal muscle fibres, greater oxygen consumption and enhanced fatty acid oxidation at thermoneutrality[36]. These findings suggest that chronically elevated SLN levels in skeletal muscle can lead to a higher basal metabolic rate. In contrast, our study observed that SLN expression slightly increased during the sedentary phase but dramatically surged after exercise in *cFeimin* MKO mice. Notably, the deletion of *cFeimin* mice had no discernible effects on the basal metabolic rate. Consequently, the loss of *cFeimin* results in an acute upregulation of SLN during exercise, which enhances thermogenesis and impairs exercise capacity as a mechanism to prevent overheating. Beyond its role in muscle contraction, SLN has also been implicated in thermogenesis independent of muscle contraction[29,35,36]. Studies suggest that SLN may be a crucial mediator of muscle thermogenesis during cold exposure, influencing energy expenditure and resistance to diet-induced obesity[29,35,36]. Our data indicate that *cFeimin* MKO mice display significantly increased *Sln* levels, leading to increased heat production during exercise. Consequently, the elevated heat production inhibits muscle performance. Furthermore, knockdown of *Sln* in *cFeimin* MKO mice can decrease the heat production and rescue the exercise capacity in *cFeimin* MKO mice. Mechanistically, the increased SLN levels inhibit cytosolic calcium reflux and improve OXPHOS, which is consistent with previous studies[35,36].

At moderate exercise intensities of ~50–70% VO_2 max, both fat and carbohydrate contribute substrate from stores inside and outside the muscle. Muscle glycogen, as one of the important energy depots in skeletal muscle, is essential for exercise[8]. Muscle glycogen in *cFeimin* MKO mice was lower than in WT mice. This may be a reason for the decreased exercise capacity in *cFeimin* MKO mice. Although muscle glycogen levels were comparable in WT and *cFeimin* MKO mice after AICAR treatment, AICAR treatment did not rescue exercise capacity in *cFeimin* MKO mice. In addition, *Sln* knockdown in *cFeimin* MKO mice did not affect muscle glycogen levels, but it restored exercise performance. Consistent with these results, *Foxc2* MKO mice exhibited similar muscle glycogen levels but significantly enhanced exercise performance. Higher energy expenditure in *cFeimin* MKO mice and lower energy expenditure in *Foxc2* MKO mice were negatively correlated with mouse exercise performance. It is possible that energy waste accounts for the diminished exercise performance. In support of this notion, knockdown of *Sln* in *cFeimin* MKO restored exercise capacity. Together, these results indicate that muscle thermogenesis, rather than glycogen levels, may play a critical role in cFeimin-mediated exercise performance.

FOXC2, a member of the forkhead/winged helix transcription factor family, plays a crucial role in regulating embryonic development, adipocyte metabolism, arterial specification, vascular sprouting and muscle regeneration[49–53]. While previous research indicated that FOXC2 regulates C2C12 differentiation and is increased during muscle regeneration[53], its function in mature adult muscle metabolism remained unknown. Our data reveal that FOXC2 binds to cFeimin. Notably, the deletion of *Foxc2* in mature skeletal muscle had no discernible impact on muscle development and fibre-type reprogramming. However, it significantly promoted muscle exercise capacity by reducing unnecessary energy consumption. By overexpressing cFeimin in *Foxc2* MKO mouse skeletal muscle tissue, we demonstrated that cFeimin inhibits *Sln* expression to reduce exercise performance through the action of FOXC2.

Furthermore, our study highlights the pivotal role of AMPK in regulating ATP consumption during exercise. AMPK, activated in response to muscle contraction and exercise, orchestrates a cascade of phosphorylation events involving various downstream metabolic enzymes[5,7,10,12–16]. This process effectively curtails anabolic pathways that consume ATP while concurrently activating catabolic pathways that generate ATP. Remarkably, our research has unveiled a facet of AMPK's functionality (its ability to phosphorylate cFeimin), thereby inhibiting the expression of the thermogenesis gene *Sln*. This regulatory mechanism operates as a crucial energy-balancing process during exercise, where SLN, as a key thermogenesis regulator, would otherwise promote ATP consumption. Studies have shown that the deletion of AMPKα in muscle resulted in impaired exercise capacity, diminished mitochondrial function and reduced contraction-stimulated utilization of muscle glycogen, glucose and fatty acids[38,41]. Compared with AMPKα1, AMPKα2 plays a major role in muscle metabolism[39]. Mice expressing the kinase-dead AMPKα2 subunit show markedly impaired exercise tolerance[42,54]. However, there is still controversy over whether AMPK is necessary for exercise-regulated muscle glucose uptake[42,54–57]. In addition, mice with tamoxifen-induced acute muscle-specific double KO of AMPKα1/AMPKα2 displayed diminished exercise capacity, reduced muscle glycogen content and depleted muscle ATP, whereas muscle mitochondrial respiration, whole-body substrate utilization and muscle glucose uptake and fatty acid oxidation during muscle contractile activity remained unaffected[40]. These studies indicate that acute loss of AMPK mainly results in reduced glycogen storage and depletion of ATP, while chronic loss of AMPK may lead to additional defects in utilization of multiple energy substrates and impairment of mitochondrial function. Our data show significantly reduced exercise performance accompanied by increased body temperature and *Sln*

Fig. 6 | AMPK phosphorylates cFeimin and promotes its nuclear translocation. **a**, The AMPK inhibitor Compound C (8 mg kg^{-1} for 24 h) effectively prevents the exercise-induced nuclear translocation of cFeimin. $n = 6$ male mice. **b**, Identification of cFeimin Thr128 phosphorylation by liquid chromatography mass spectrometry (LC–MS/MS) analysis. **c**, An amino acid sequence alignment of cFeimin orthologues reveals conservation of two potential phosphorylation sites, indicated by the red arrows. Thr112 was identified by motif scanning and Thr128 was identified by LC–MS/MS. These two Thr (T) residues were mutated to Ala (A) to create the cFeimin T/A mutant. **d**, An in vitro kinase assay demonstrates the phosphorylation of His-tagged WT cFeimin, but not the T/A mutant, by AMPK. **e**, Immunoblots (left) and statistical data (right) illustrate the phosphorylation of cFeimin in gastrocnemius muscle extracts from male mice injected with PBS (Veh) or Compound C (Comp, 8 mg kg^{-1} for 24 h) under sedentary (Sed) or 90-min exercise (Exe) conditions. $n = 3$ biological replicates. **f**, Immunostaining (left) and quantification (right) depict the cellular localization of WT, T/A and T/D cFeimin in HEK293T cells in the presence or absence of Compound C. T/A is the phosphorylation-mimic cFeimin mutant carrying T112A and T128A substitutions in HEK293T cells and T/D is the phosphorylation-mimic cFeimin mutant carrying T112D and T128D substitutions in HEK293T cells. $n = 12$ cells. **g**, Immunostaining (left) and quantification (right) demonstrate the cellular localization of WT, T/A and T/D cFeimin in gastrocnemius muscle of male mice under sedentary (Sed) or 90-min exercise (Exe) conditions. $n = 6$ mice. **h**, ChIP–qPCR showing the effect of WT, T/A and T/D cFeimin on FOXC2-binding capacity within the *Sln* promoter in *cFeimin* WT (*cFeimin*$^{+/+}$) and KO (*cFeimin*$^{-/-}$) myotubes. $n = 4$ biological replicates. **i**–**k**, The effects of WT, T/A and T/D cFeimin on *Sln* expression (**i**), cellular Ca^{2+} levels (**j**) and OCR and statistical analyses of baseline respiratory capacity, ATP-coupled respiratory capacity and maximum respiratory capacity (**k**) in differentiated *cFeimin* WT (*cFeimin*$^{+/+}$) and KO (*cFeimin*$^{-/-}$) myotubes. $n = 4$ biological replicates (**i**), $n = 22$ cells (*cFeimin*$^{+/+}$, **j**), $n = 21$ cells (*cFeimin*$^{-/-}$, **j**), $n = 18$ cells (*cFeimin*$^{-/-}$ + WT, **j**), $n = 19$ cells (*cFeimin*$^{-/-}$ + T/A, **j**), $n = 21$ cells (*cFeimin*$^{-/-}$ + T/D, **j**), $n = 5$ biological replicates (*cFeimin*$^{+/+}$, **k**), $n = 7$ biological replicates (*cFeimin*$^{-/-}$, **k**), $n = 6$ biological replicates (*cFeimin*$^{-/-}$ + WT, **k**), $n = 8$ biological replicates (*cFeimin*$^{-/-}$ + T/A, **k**), $n = 8$ biological replicates (*cFeimin*$^{-/-}$ + T/D, **k**). Data are shown as mean ± s.e.m. Statistical comparisons were performed using two-way ANOVA followed by Tukey's test (**a**,**e**–**i**,**k**). All individual points and *P* values are shown.

https://doi.org/10.1038/s42255-024-01176-8

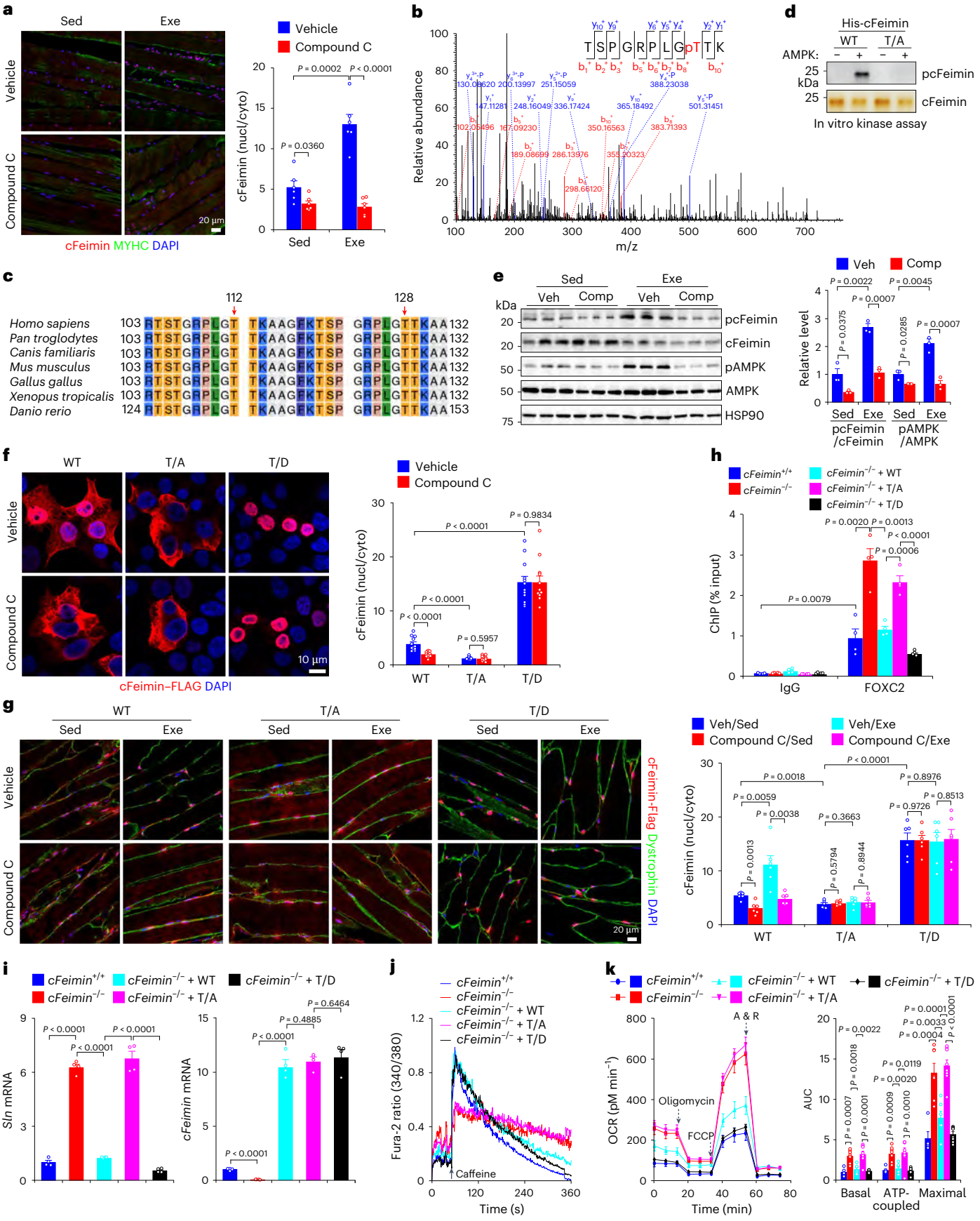

https://doi.org/10.1038/s42255-024-01176-8

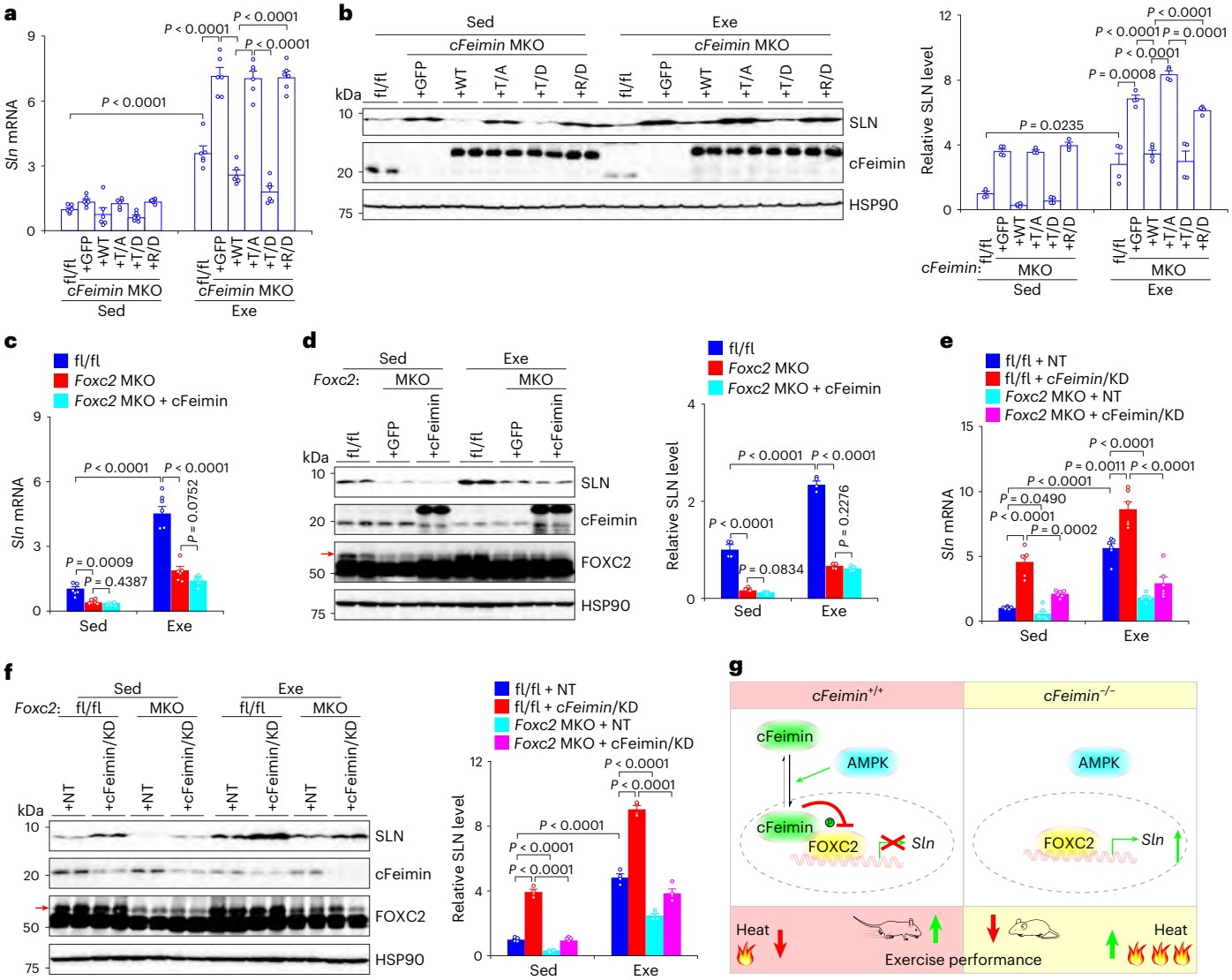

Fig. 7 | cFeimin binds to FOXC2 and suppresses muscle thermogenesis. **a**,**b**, qPCR results (**a**) and immunoblots and statistical data (**b**) showing the effect of WT cFeimin, T/A cFeimin (phosphorylation-defective mutant), T/D cFeimin (phosphorylation-mimic mutant) or R/D cFeimin (FOXC2-binding-defective mutant) on SLN expression in gastrocnemius muscle extracts from male *cFeimin* WT (fl/fl) or MKO mice under sedentary (Sed) or 90-min exercise (Exe) conditions. $n = 6$ mice (**a**), $n = 4$ biological replicates (**b**). **c**,**d**, qPCR results (**c**) and immunoblots and statistical data (**d**) showing the effect of cFeimin overexpression on SLN expression in gastrocnemius muscle extracts from male *Foxc2* WT (fl/fl) or MKO mice under sedentary (Sed) or 90-min exercise (Exe) conditions. On the immunoblot, FOXC2 is denoted by the red arrow. $n = 6$ mice (**c**), $n = 4$ biological replicates (**d**). **e**,**f**, qPCR results (**e**) and immunoblots and statistical data (**f**) showing the effect of *cFeimin* knockdown (KD) on SLN expression in gastrocnemius muscle extracts from male *Foxc2* WT (fl/fl) or MKO mice under sedentary (Sed) or 90-min exercise (Exe) conditions. On the immunoblot, FOXC2 is denoted by the red arrow. NT, non-targeting shRNA. $n = 6$ mice (**e**), $n = 4$ biological replicates (**f**). **g**, In WT (*cFeimin*$^{+/+}$) mice, exercise activates AMPK, promoting the phosphorylation and nuclear translocation of cFeimin. Nucleus-localized cFeimin interacts with FOXC2, suppressing *Sln* expression. Consequently, cFeimin reduces muscle heat production, thereby enhancing exercise performance. However, *cFeimin* deficiency relieves the inhibitory effect of cFeimin on FOXC2-controlled *Sln* expression and disrupts the SLN-mediated modulation of heat production and exercise performance. Data are shown as mean ± s.e.m. Statistical comparisons were performed using two-way ANOVA followed by Tukey's test (**a**–**f**). All individual points and *P* values are shown.

expression in AMPKα1/AMPKα2 MKO mice during exercise. Numerous AMPK activators, among them AICAR, have been previously shown to enhance exercise endurance[43]. In line with our findings, it is likely that AICAR achieves this effect by engaging the cFeimin–FOXC2–SLN signalling axis. This suggests that AICAR boosts exercise performance through the concerted action of cFeimin, FOXC2 and SLN. Notably, our data also indicate that AMPK exerts a fine-tuned control over ATP consumption during exercise through the phosphorylation of cFeimin. This metabolic pathway expands our understanding of AMPK's multifaceted role in regulating energy dynamics during physical activity.

In conclusion, our study reveals a cFeimin–FOXC2–SLN signalling axis that integrates AMPK signalling to regulate muscle exercise performance, at least in part by modulating muscle thermogenesis. It expands our understanding of the physiological regulation of exercise performance and may have implications for the treatment of muscle metabolic disorders. Considering the increased energy consumption observed in *cFeimin* MKO mice, it becomes imperative to conduct further research to investigate whether cFeimin, acting as a regulator of exercise performance in muscle, might also confer resistance to conditions such as obesity, insulin resistance and type 2 diabetes.

https://doi.org/10.1038/s42255-024-01176-8

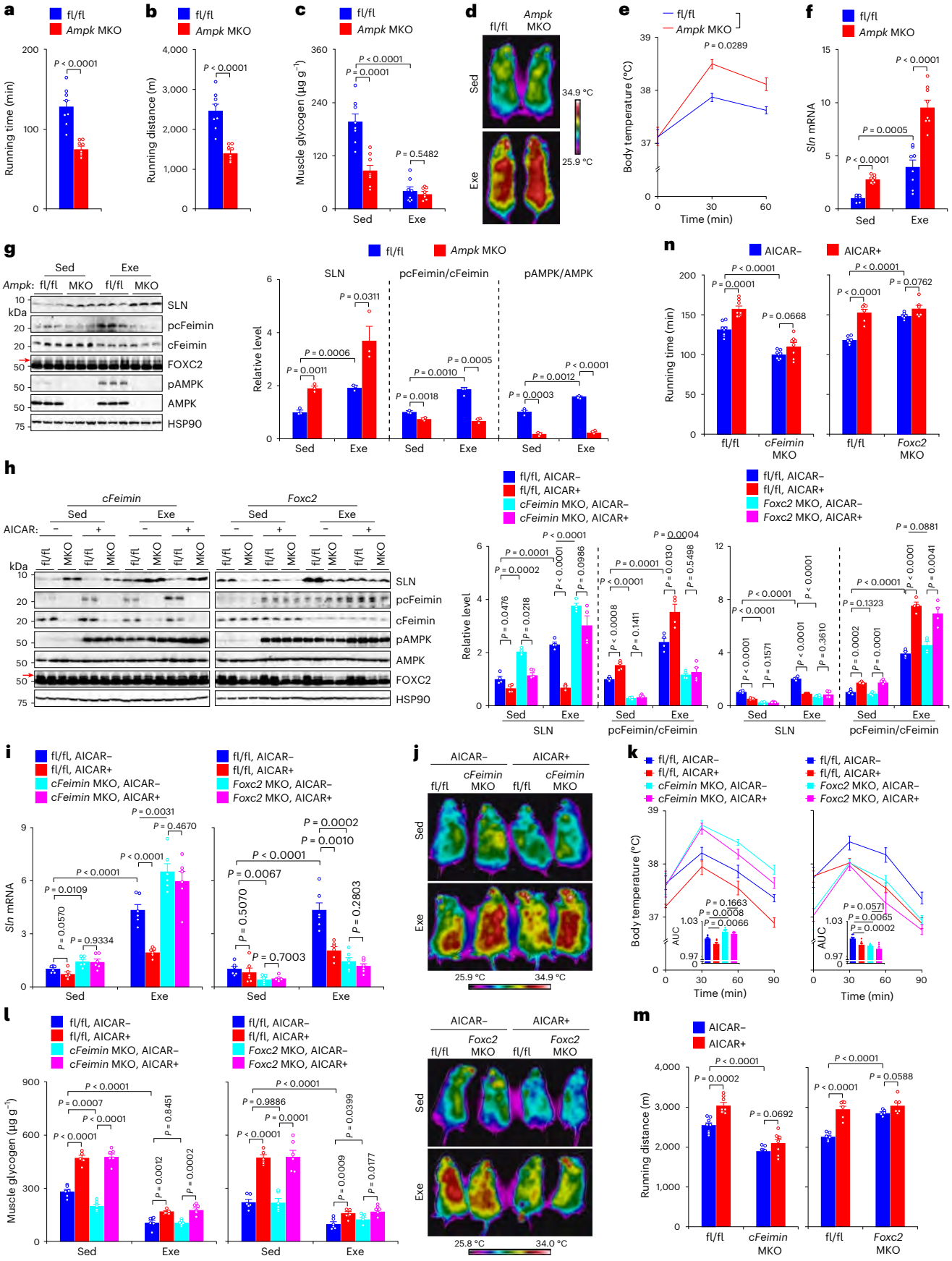

Fig. 8 | AMPK enhances exercise performance through cFeimin and FOXC2. **a**,**b**, Running time (**a**) and running distance (**b**) of 10-week-old male WT (fl/fl) and AMPKα1&2 (*Ampk*) MKO mice. $n = 8$ mice. **c**, Muscle glycogen levels in male fl/fl and *Ampk* MKO mice before (sedentary (Sed)) or after 60 min of exercise (Exe). $n = 8$ mice. **d**,**e**, Body surface temperature (**d**) and rectal temperature (**e**) of male fl/fl and *Ampk* MKO mice were monitored during exercise. $n = 8$ mice (**e**). **f**,**g**, qPCR (**f**) and immunoblotting and statistical data (**g**) showing SLN expression and phosphorylation of AMPK and cFeimin in gastrocnemius muscle extracts from male fl/fl and *Ampk* MKO mice under sedentary conditions (Sed) or after 60 min of exercise (Exe). $n = 8$ mice (**f**), $n = 3$ biological replicates (**g**). **h**–**n**, The effects of AICAR on *Sln* expression (**h**,**i**), body surface temperature (**j**), rectal temperature (**k**), glycogen level (**l**) and running capacity (**m**,**n**) in male fl/fl, *cFeimin* MKO mice or *Foxc2* MKO mice. Mice were intraperitoneally injected with AICAR (500 mg $kg^{-1}day^{-1}$) for 2 weeks. On the immunoblots, FOXC2 is denoted by the red arrow. $n = 4$ biological replicates (**h**), $n = 6$ mice (**i**), $n = 8$ mice (**k**), $n = 6$ mice (**l**), $n = 8$ mice (*cFeimin* MKO, **m**,**n**), $n = 6$ mice (*Foxc2* MKO, **m**,**n**). Data are shown as mean ± s.e.m. Statistical comparisons were performed using an unpaired two-tailed Student's *t*-test (**a**,**b**) or two-way ANOVA followed by Tukey's test (**c**,**e**–**i**,**k**–**n**). All individual points and *P* values are shown.

Methods

Mouse strains and experiments

Mice were housed in a temperature-controlled environment at around 21 °C with free access to food and water using a 12-h light–dark cycle. All mice were maintained on a C57BL/6J background and fed with chow diet (1010058, Jiangsu Xietong Pharmaceutical Bio-engineering Co.). Animals were maintained with all relevant ethical regulations for animal testing and research. All animal experiments were approved by the Animal Care and Use Committee at Tsinghua University.

AMPKα1/AMPKα2 (*Ampk*) MKO mice and *Ucp1*$^{-/-}$ mice were previously reported[58,59].

Mice carrying a floxed allele of *cFeimin* and *Foxc2* were obtained from Viewsolid Biotech and GemPharmatech, respectively. For generation of *cFeimin* MKO and *Foxc2* MKO mice, *cFeimin*$^{fl/fl}$ mice and *Foxc2*$^{fl/fl}$ mice were crossed with mice expressing the Cre-recombinase transgene from the muscle-specific human α-skeletal actin promoter (*Hsa-Cre*). PCR genotyping of *cFeimin* MKO and *Foxc2* MKO mice was performed with the following allele-specific primers: c*Feimin* LoxP, forward 5′-TGTGGTGTGACTTTTTGGGGAAGGC-3′; and reverse 5′-AAGCATACTGTTCCACGACAGCGAC-3′. *Foxc2* LoxP, forward 5′-TTCTGCTCTTTACACAAACACAGC-3′; and reverse 5′-TG TGGCTGCCTATCCAACCTG-3′. *HSA-Cre*, forward 5′-GCCTGCATTAC CGGTCGATGC-3′; and reverse 5′-CAGGGTGTTATAAGCAATCCC-3′.

Global genetic ablation of *cFeimin* was achieved by injection of a mixture of Cas9 mRNA (100 ng μl^{-1}) and two sgRNAs (5′-GTT GCCGGCAGTAATCCAGC-3′ and 5′-CCCAGCAAAACAAGTACAGC-3′; 50 ng μl^{-1} each). Cleaved embryos with high quality at the two-cell to blastocyst stage were transferred into the oviduct of matched recipient mice. Heterozygous mice carrying the deleted c*Feimin* allele were crossed to each other to generate knockout mice. Genotypes were confirmed by PCR using the following primers: c*Feimin*: 5′-TGGAGTCTACCCTATTGCCC-3′ and 5′-TCGCTTACCA GATCGATTGAGG-3′.

Indirect calorimetry, physical activity and food intake

To measure the energy metabolism of the mice in ad libitum conditions, energy expenditure, RER, physical activity and food intake were simultaneously measured for individually housed mice with a PhenoMaster system (TSE Systems) as previously described[60]. Mice were allowed to acclimatize in the chambers for at least 72 h. Food and water were provided ad libitum in the appropriate devices and measured by the built-in automated instruments.

Measurement of body temperature

The core body temperature of mice was measured using a BAT-12 microprobe thermometer (BAT-12, Physitemp). The surface temperature of the mice was imaged using a high-resolution infra-red camera (FLIR C5-c51.1).

Gripping test

The gripping force of the mice was assessed using a method previously described[61]. The procedure involved setting up a grip strength meter (GSM) on a stable and level surface. The GSM was then connected to a digital force gauge. Mice were carefully placed on top of the grid, allowing them to grip the grid with all four paws. The peak force exerted by the mouse was recorded as soon as it released its grip from the grid. This value was displayed on the screen of the GSM.

In vivo metabolic assays

Metabolic assays were performed as previously described[60,62]. In brief, blood glucose values were determined using a LifeScan automatic glucometer. Triglycerides (TR0100, Sigma), ATP (S0026, Beyotime) and glycogen (MAK016, Sigma-Aldrich) were measured according to the manufacturer's instructions.

Measurement of oxygen consumption rates

Cellular OCRs were measured using the Seahorse XFe96 analyzer (Agilent). To measure myotube respiration, myoblasts were initially seeded on Matrigel-coated plates and allowed to differentiate for 3 days within Seahorse XFe96 microplates. One hour before commencing the assay, myotubes were transitioned to a medium comprising DMEM supplemented with 2.5 mM glucose (G7528, Sigma-Aldrich), 4 mM L-glutamine (G8540, Sigma-Aldrich) and 1 mM sodium pyruvate (S8636, Sigma-Aldrich). The respiration rates were recorded three times, followed by successive injections of oligomycin (2 μM, ab141829, Abcam), the uncoupler FCCP (1.5 μM, C2920, Sigma-Aldrich) and rotenone (1 μM, R8875, Sigma-Aldrich)/antimycin (1 μM, ab141904, Abcam). Immediately following the measurements, total protein levels were quantified using the Pierce BCA Protein Assay kit (23225, Thermo Fisher). Subsequently, the OCR data were normalized to the protein content.

Exercise test and maximal oxygen consumption test

Mice were acclimatized to the treadmill for three consecutive days at low speed (10 m min^{-1}) with a 5° incline for 10 min. Exercises were performed as described previously. High-intensity exercise sessions started at 10 m min^{-1} for the initial 10 min, with increments of 2 m min^{-1} every 5 min until the mice reached exhaustion. In contrast, low-intensity exercise sessions started at 10 m min^{-1} for the initial 10 min, followed by a consistent speed of 20 m min^{-1} until the mice reached exhaustion. Exhaustion was defined as the inability to stay on the electrical shockwave plate for more than 5 s. Measurement of O_2, CO_2 and RER during exercise was carried out using the following method: The mice were placed in an enclosed treadmill integrated with a PhenoMaster system (TSE Systems) for a 5-min period at a 5° incline and 0 m min^{-1}. To determine maximal exercise capacity, mice underwent a high-intensity exercise test, which involved increasing the speed every 2 min at a 5° incline until they reached exhaustion. Following a 1-week interval, the same group of mice participated in a low-intensity exercise challenge. After a brief warm-up, the mice were subjected to a constant speed of 60% of their maximal running speed (20 m min^{-1}) at a 5° incline until they reached exhaustion. Measurements were taken both before the exercise challenge and throughout the challenge itself.

RNA-seq and data processing

Total RNA extraction was conducted using the GeneMark Total RNA Purification kit. To assess RNA quality, a NanoDrop ND2000 spectrophotometer from Thermo Scientific was employed. Subsequently,

18 libraries were meticulously prepared by BGI Genomics, and all samples were sequenced on the DNBSEQ platform. In total, 18,995 genes were identified. The RNA-seq data, consisting of 50-bp single-end reads from the DNBSEQ platform, underwent initial preprocessing, including the removal of adaptor sequences and quality assessment using the FastQC tool (v.0.12.1). Sequencing data were demultiplexed and subjected to primary analysis utilizing SOAPnuke (v.1.5.2), followed by alignment to the mouse reference genome (GRCm38.p6) using HISAT2 (v.2.2.1)[63]. SAMtools (v.1.9) was employed to sort and index the alignment BAM files, while StringTie (v.2.1.4) was used for read counting within gene ranges, utilizing Ensembl mouse gene annotation v.102.38. Alignment quality and statistics were assessed using SAMstat (v.1.5.2), revealing an alignment rate ranging from 92% to 95% for the samples in this study. Subsequently, the count vectors from all samples were consolidated into a table, which then underwent secondary analysis in R (v.4.3). Quality control and sample consistency were assessed through principal-component analysis using the R package PCATools (v.2.14.0). The count table was further processed in the secondary statistical analysis using R scripts with DESeq2 (v.1.40.2)[64]. A maximum likelihood estimate model with contrast tests was specifically employed in our analysis. This approach resulted in lists of genes ranked for differential expression, which were based on Wald test *P* values. Benjamini–Hochberg-adjusted *P* values were utilized to estimate the false discovery rate, providing a robust method for identifying significant gene expression changes. Differential expression was defined with a cutoff of $\log_2$ fold change (logFC) of ±1 and a *P* value < 0.05. Significant gene lists were subsequently subjected to clusterProfiler (v.4.7.1)[65]. Genes were pre-ranked according to their fold change in expression, and the application scored this sorted gene list regarding its enrichment in selected functional categories, such as GO. The significance of the enrichment score was assessed via 1,000 permutations and Benjamini–Hochberg's false discovery rate was calculated for multiple testing adjustments. Significance was defined as a *q*-value < 0.05. The enriched pathways were then visualized using the plot module within this application. The dataset has been deposited in the NCBI Gene Expression Omnibus database (GSE280845).

AAV injection

cFeimin–3×Flag–AAV9, cFeimin 112/128T/A–3×Flag–AAV9, cFeimin 112/128T/D–3×Flag–AAV9, cFeimin 124/140R/D–3×Flag–AAV9 and shRNA cFeimin–AAV9 (5′-ATCTGTATTCCTCCCAGCAAA-3′) were made by WZ Biosciences. The AAVs were injected into gastrocnemius muscle with 5×10^{11} viral genomes in 80 µl PBS. After 2 months, mice were trained and the gastrocnemius muscle was collected. The shRNA *Sln* (5′-GCTTTGTTCCCTAGCAAATGT-3′) and sh-NC (5′-TTCTCCGAACGTGTCACGT-3′) were ligated into the linearization vector pAAV-U6-shRNA/spgRNA v2.0-CMV-EGFP-WPRE (OBiO Technology). These AAVs were packaged into the MyoAAV1A vector, which is specific for delivery to skeletal muscle[66]. Approximately 1×10^{11} viral genomes of MyoAAV vectors were administered to mice by tail-vein injection. Mice were collected after 1.5 months.

Adenovirus preparation

The cFeimin–3×Flag, cFeimin 112/128T/A–3×Flag, cFeimin 112/128T/D–3×Flag, cFeimin 124/140R/D–3×Flag, cFeimin ΔNLS–3×Flag and FOXC2–3×HA were cloned into the pAdTrack–CMV vector. Following sequencing, the correct plasmid was subjected to Pme1 digestion and subsequently introduced into pAdEasy competent cells. The identification of positive recombinant plasmids was achieved through Pac1 digestion. Next, 10 µg of linearized recombinant plasmid was transfected into 293A cells cultured in a 10-cm dish using Lipofectamine Plus (Invitrogen). After a period of 7–10 days, the cells were collected and the recombinant adenovirus was extracted through three cycles of freeze-thaw vortexing. To amplify the adenovirus, two additional rounds of 293A cell infection were carried out. Additionally, a recombinant adenovirus containing the empty pAdTrack–CMV plasmid was generated to serve as a control for experimental purposes.

Cell culture

HEK293T cells were maintained at 37 °C and 5% CO_2 in DMEM high-glucose medium (10-013-CVRC, Corning) containing 10% FBS (SE00-011, Vistech) and 100 mg ml^{-1} penicillin–streptomycin (60162ES76, Yeasen Biotech). Human Skeletal Muscle Cells (CP-H095, Pricella) were maintained at 37 °C and 5% CO_2 in DMEM high-glucose medium (10-013-CVRC, Corning) with basic fibroblast growth factor (C751, Novoprotein), 10% GlutaMAX (A12860-01, Gibco), 10% FBS (SE00-011, Vistech) and 1% penicillin–streptomycin (60162ES76, Yeasen Biotech). For differentiation, 2% horse serum (16050130, Thermo Fisher Scientific) was added to DMEM high-glucose medium for 72 h. All cell lines were routinely tested for mycoplasma using a PCR detection kit (MP0035, Sigma).

Isolation and culture of mouse primary myoblast cells

Primary myoblasts were isolated from the hindlimb skeletal muscles of 1-month-old mice, including those of WT, *cFeimin* KO or *Foxc2* fl/fl mice. The detailed procedure involved carefully dissecting the muscles, mincing them into approximately 1-mm^3 pieces and subjecting them to a 20-min enzymatic digestion using a mixture of Collagenase D (0.75 U ml^{-1}) and Dispase II (1 U ml^{-1}) in the presence of 2.5 mM $CaCl_2$. The enzymatic reaction was halted by adding F-10 medium with 20% FBS. After filtration and centrifugation, the collected cells were cultured for 3 days in F-10 Ham's medium supplemented with 20% FBS, 4 ng ml^{-1} of basic fibroblast growth factor and 1% penicillin–streptomycin. Following this initial culture period, myoblasts were isolated by trypsin treatment and transferred to a non-coated culture plate. After 1 h, the supernatant was transferred to a collagen-coated plate. Pure myoblast populations were obtained through several generations of pre-plating. For differentiation, primary myoblasts were seeded on Matrigel-coated cell culture plates and induced to differentiate by replacing the culture medium with DMEM containing 2% horse serum and 1% penicillin–streptomycin when the cell density reached 90%.

Lentivirus-mediated *Sln* knockdown

The shRNA targeting *Sln* (5′-GCTTTGTTCCCTAGCAAATGT-3′) was designed using the online software available at https://rnaidesigner.invitrogen.com/rnaiexpress/. The annealed shRNA was then inserted into the pLKO.1 vector. Subsequently, this construct, along with pCMV-VSVG, REV and PMD2 plasmids, was co-transfected into HEK293T cells cultured in a 10-cm dish. Following a 48-h transfection period, the culture medium was filtered through a 0.45-µm filter to remove cellular debris and the lentivirus was collected. To establish stable knockdown cells targeting *Sln*, WT and *cFeimin* MKO myoblasts (at 50% confluence) were infected with either *Sln*-specific or scramble shRNA lentivirus. After 48 h of infection, puromycin (S7417, Selleck) was introduced at a concentration of 1 µg ml^{-1} in the culture medium to select for shRNA-expressing cells. Puromycin was maintained in the culture medium for two generations to obtain a pure population of lentivirus-infected cells.

Chemical treatment

For chemical treatment of mice, Dorsomorphin 2HCl (Compound C) (S7306, Selleck) was injected into gastrocnemius muscle at 8 mg kg^{-1} and the animals were analysed 24 h after injection. AICAR (S1802, Selleck) was injected into the abdomen at 500 mg $kg^{-1}day^{-1}$ for 2 weeks. For chemical treatment of cells, myotubes were treated with AICAR (1 mM), GW1516 (100 nM, HY-10838, MedChemExpress), SR9009 (10 µM, HY-16989, MedChemExpress) and trimetazidine (150 µM, HY-B0968A, MedChemExpress) for 3 h. HEK293T were treated with Compound C (20 µM) for 8 h.

gRNA design and generation of primary myoblasts with targeted deletions in the *Sln* promoter

Two guide RNAs (gRNAs) were designed using CHOPCHOP (https://chopchop.cbu.uib.no/). One gRNA (5′-TTGCAAACAGCTAGTGATAG-3′) specifically targeted the region −409 to −390 upstream from the transcription start site (TSS) of *Sln*. Another gRNA (5′-CCACTACA TCAAAAGTAGGC-3′) specifically targeted the region −234 to −215 upstream from the TSS of *Sln*. These gRNA sequences were cloned into the PX458 vector (48138, Addgene). Both gRNA expression plasmids were simultaneously transfected into mouse primary myoblasts using Lipofectamine 2000 according to the manufacturer's protocol. The culture medium was changed 12 h after transfection. After 48 h, the myoblasts were trypsinized, washed with PBS, and resuspended in PBS/1% FBS for single-cell sorting based on green fluorescent protein expression using fluorescence-activated cell sorting into a 96-well plate containing complete medium. Clonal cell lines were expanded and screened by PCR amplification of the protospacer adjacent motif (PAM). Genomic DNA from the clonal cell lines was purified using the AxyPrep Multisource Genomic DNA Miniprep kit (AP-MN-MS-GDNA-250G, Axygen) following the manufacturer's protocol. The region surrounding the PAM was then amplified using 2× Phanta Max Master Mix (P515, Vazyme) with the following primers: *Sln*-forward: 5′-ACTTGCTGGGCATTGCTTTG-3′; *Sln*-reverse: 5′-CCTCAGTCTCTCCACCTCCA-3′. The PCR products were subsequently purified using the AxyPrep PCR Cleanup kit (AP-PCR-250, Axygen) for sequencing analysis.

Calcium imaging

Myotubes cultured on 12-mm round glass coverslips coated with Matrigel were initially rinsed with Krebs–Ringer–HEPES buffer (125 mM NaCl, 5 mM KCl, 1.2 mM KH_2PO_4, 6 mM glucose, 1.2 mM $MgCl_2$, 25 mM HEPES and 1.5 mM Ca^{2+}). Subsequently, they were incubated with 2.5 μM Fura-2-AM (F1221, Life Technologies) in the presence of 0.05% Pluronic F-127 (P3000MP, Life Technologies) for 30 min at 37 °C. To release the accumulated Ca^{2+} from the SR, 10 mM caffeine (500 μM, A10431, Thermo Fisher) was applied. Images of Fura-2-loaded myotubes were captured using a CoolSNAP CCD camera and Lambda XL light box from Sutter Instrument. During image acquisition, the excitation wavelength alternated between 340 nm and 380 nm. The ratio of fluorescence intensity at the two excitation wavelengths was determined after subtracting the background fluorescence. All images were collected and analysed using the MetaFluor software (v.7.10.4.407) package from Molecular Devices.

Immunoprecipitation and immunoblotting

Cell lysates were prepared from cultured cells using a cell lysis buffer comprising 150 mM NaCl, 50 mM HEPES at pH 7.4, 1% Triton X-100 and 10% glycerol. This lysis buffer also contained a cocktail of protease and phosphatase inhibitors (B15001 and B14001, Bimake). For immunoprecipitation using anti-Flag beads (A2220, Sigma) and anti-HA beads (26182, Thermo Scientific), cell lysates were incubated with agarose beads conjugated with the anti-Flag and anti-HA antibody overnight at 4 °C. Subsequently, the antibody-bound beads were washed five times with cell lysis buffer and then boiled for 10 min in loading buffer.

For immunoblotting, cell lysates were prepared using RIPA lysis buffer (50 mM Tris-HCl, pH 8.0, 1 mM EDTA, 0.5 mM EGTA, 1% Triton X-100, 0.1% sodium deoxycholate and 140 mM NaCl). This lysis buffer also included a cocktail of protease and phosphatase inhibitors. Protein concentrations were determined using the BCA Protein Assay kit (23225, Thermo Fisher). Subsequently, samples were loaded onto SDS–PAGE gels and then transferred to nitrocellulose membranes.

Immunoblotting was carried out in a gelatin buffer composed of 50 mM Tris-HCl, pH 7.4, 150 mM NaCl, 5 mM EDTA and 0.05% Tween-20, using the appropriate antibodies. The antibodies were purchased and diluted as follows: anti-Feimin (PA5-66500, 1:1,000, Invitrogen); anti-AMPKα (2532, 1:1,000), anti-pAMPKα (2535, 1:1,000), anti-HSP90 (4874S, 1:1,000) and anti-UCP1 (14670, 1:1,000) from Cell Signaling Technology; anti-SERCA1a (22361, 1:1,000), anti-SERCA2a (67248, 1:1,000) and anti-UCP2 (11081-1, 1:1,000) from Proteintech; anti-UCP3 (A1532, 1:1,000, ABclonal); anti-SLN (ABT13, 1:1,000, Sigma-Aldrich); and anti-FOXC2 (sc-515234, 1:1,000, Santa Cruz). Goat anti-mouse IgG (H+L)-HRP conjugate (1706516, 1:5,000) and goat anti-rabbit IgG (H+L)-HRP conjugate (1706515, 1:5,000) were from Bio-Rad. The rabbit polyclonal anti-pcFeimin antibody (1:1,000) was generated and purified by ABclonal.

Immunofluorescence in muscle tissues and cell lines

For immunostaining, tissue sections or cultured cells were initially fixed in 4% paraformaldehyde (PFA) for a duration of 10 min. Subsequently, they were quenched with 100 mM glycine for another 10 min. Following this, the samples were immersed in blocking buffer (5% goat serum, 2% BSA, 0.1% Triton X-100 and 0.1% sodium azide in PBS) for 2 h. Next, the samples were incubated with the following primary antibodies: anti-FLAG (1:1,000 dilution, F1804, Sigma-Aldrich); anti-MYHI (1:200 dilution, BA-D5s, DHSB); MYHIIa (1:200 dilution, SC-71, DHSB); MYHIIX (1:200 dilution, 6H1, DHSB); MYHC (1:200 dilution, MF 20, DHSB), dystrophin (1:1,000 dilution, ab15277, Abcam) and cFeimin (1:1,000 dilution) at 4 °C overnight. Subsequently, secondary antibodies were applied to the samples at room temperature for 1 h. The antibodies were purchased and diluted as follows: goat anti-mouse IgG1, Alexa Fluor 568 (A-21124, 1:1,000, Thermo Fisher Scientific); goat anti-mouse IgG2b, Alexa Fluor 647 (A-21242, 1:1,000, Thermo Fisher Scientific); goat anti-mouse IgM, Alexa Fluor 488 (A-21042, 1:1,000, Thermo Fisher Scientific); goat anti-mouse, Alexa Fluor 546 (A-11003, 1:1,000, Thermo Fisher Scientific); donkey anti-rabbit, Alexa Fluor 488 (A21206, 1:1,000, Thermo Fisher Scientific) and donkey anti-rabbit IgG, Alexa Fluor 555 (A-32816, 1:1,000, Thermo Fisher Scientific). The rabbit polyclonal anti-cFeimin (1:1,000) antibody used in this procedure was generated and purified by ABclonal.

RNA extraction and quantitative PCR

Total RNA extracted from whole gastrocnemius, brown adipose tissues and myotubes was isolated using the FastPure Cell/Tissue Total RNA Isolation kit V2 (RC112-01, Vazyme). Subsequently, cDNA was synthesized using the Hifair III First Strand cDNA Synthesis SuperMix for qPCR (11141ES60, Yeasen). RNA levels were quantified with the LightCycler 480 II (Roche). The following primers were used for qPCR:

*Ampk*α1-forward: 5′-ACCTGAGAACGTCCTGCTTG-3′
*Ampk*α1-reverse: 5′- GAAATGACTTCTGGTGCGGC-3′
*Ampk*α2-forward: 5′- CCGAGGGGGTGTGTTTTACA-3′
*Ampk*α2-reverse: 5′- GGTAGCTGGGCAAATCCTGT-3′
cFeimin-forward: 5′-GGCCGGAGTGAACGGAAC-3′
cFeimin-reverse: 5′-CCCACAGAACGCTGGATTAC-3′
Foxc2-forward: 5′-CGGCGCTTCAAGAAGAAGGA-3′
Foxc2-reverse: 5′-CCTCGCTCTTAACCACGACT-3′
Myh1-forward: 5′-CGGAGTCAGGTGAATACTCACG-3′
Myh1-reverse: 5′-GAGCATGAGCTAAGGCACTCT-3′
Myh2-forward: 5′-CAGAGGCAAGTAGTGGTGGAG-3′
Myh2-reverse: 5′-AAATGAGGATGGGTGCTCCTG-3′
Myh4-forward: 5′-AGGACCAACTGAGTGAAGTGA-3′
Myh4-reverse: 5′-GGGAAAACTCGCCTGACTCTG-3′
Myh7-forward: 5′-ACTGTCAACACTAAGAGGGTCA-3′
Myh7-reverse: 5′-TTGGATGATTTGATCTTCCAGGG-3′
Myod-forward: 5′-GGCTACGACACCGCCTACTA-3′
Myod-reverse: 5′-CGACTCTGGTGGTGCATCTG-3′
Myog-forward: 5′-TGCCCAGTGAATGCAACTCC-3′
Myog-reverse: 5′-TTGGGCATGGTTTCGTCTGG-3′
Pax7-forward: 5′-CTGCTGAAGGACGGTCACTG-3′
Pax7-reverse: 5′-GGATGCCATCGATGCTGTGT-3′

Rn18s-forward: 5′-GCAATTATTCCCCATGAACG-3′
Rn18s-reverse: 5′-GGCCTCACTAAACCATCCAA-3′
Sln-forward: 5′-ACTGAGGTCCTTGGTAGCCT-3′
Sln-reverse: 5′-CATGGCCCCTCAGTATTGGT-3′
Ucp1-forward: 5′-GCCAGGCTTCCAGTACCATT-3′
Ucp1-reverse: 5′-GAGGCAGGTGTTTCTCTCCC-3′
Ucp2-forward: 5′-GTGTTTCGTCTCCCAGCCAT-3′
Ucp2-reverse: 5′-TCCAGTGTCGGGAAATGCTC-3′
Ucp3-forward: 5′-ACCCGATACATGAACGCTCC-3′
Ucp3-reverse: 5′-AAAACGGAGATTCCCGCAGT-3′

Chromatin immunoprecipitation–qPCR

To achieve chromatin fragmentation of myotubes, sonication was carried out utilizing a Sonics instrument. An aliquot of chromatin was precleared with protein G (26161, Thermo Fisher Scientific) and immunoprecipitated with anti-HA beads (26182, Thermo Fisher Scientific) or IgG control (A7028, Beyotime) antibodies. After the reversal of crosslinking, DNA was isolated using the standard phenol–chloroform method. Quantitative analysis was performed by the standard curve method. Specific oligonucleotide primers for target regions were:

Sln promoter +7/−220 forward: 5′-GTAGGCCGGAAACAAGAGC TTTC-3′
Sln promoter +7/−220 reverse: 5′-GCTGTCTGAGCTCCTGGACTC-3′
Sln promoter −199/−449 forward: 5′-CGGTGTGGGAATGTG GGAAC-3′
Sln promoter −199/−449 reverse: 5′-AAAGCTCTTGTTTCCGGCCT-3′
Sln promoter −429/−598 forward: 5′-CCCATGGCTGTTTCAG GAGA-3′
Sln promoter −429/−598 reverse: 5′-TGTTCCCACATTCCCACACC-3′
Sln promoter −596/−853 forward: 5′-CCTCCCAGGCTTCTG TACAC-3′
Sln promoter −596/−853 reverse: 5′-GGGAGCCAGAGCTTG TATCCT-3′

In vitro kinase assay

Purified AMPK (0.6 µg, CT05-H0907B, Sino Biological) was incubated with various substrates (1.6 µg) in kinase reaction buffer (HEPES (H3375, Sigma-Aldrich), pH 7.4 (20 mM), dithiothreitol (D9760, Sigma-Aldrich, 1 mM), $MgCl_2$ (M0250, Sigma-Aldrich, 5 mM), EDTA (E9884, Sigma-Aldrich, 1 mM), NaF (S6776, Sigma-Aldrich, 200 µM), AMP (01930, Sigma-Aldrich, 100 mM) and ATP (A2383, Sigma-Aldrich, 100 mM)) and biotinylated ATP (HY-D0183, MedChemExpress, 200 µM) at 30 °C for 15 min. The control reactions contained no purified AMPK. Phosphorylation was detected by incorporation of biotinylated ATP using streptavidin conjugated with HRP (N100, Thermo Fisher).

Mass spectrometry

To identify proteins interacting with cFeimin, mature myotubes were cultured and infected with cFeimin–3×FLAG adenovirus. Total cell lysates were prepared for immunoprecipitation. To pinpoint phosphorylation sites on cFeimin, mature myotubes infected with cFeimin adenovirus were cultured and then treated with either dimethylsulfoxide or A769662 (S2697, Selleck) for 6 h. Total cell lysates were prepared for immunoprecipitation and the immunoprecipitation products were separated on SDS–PAGE gels. Bands within the 50–75 kDa and 75–150 kDa ranges were excised, then cut into small pieces and analysed using electrospray ionization tandem MS on a Thermo LTQ Orbitrap instrument, as previously described[60,62]. The mass spectrometry proteomics data have been deposited in the ProteomeXchange database through the PRIDE partner repository, with the dataset identifier PXD045263 and PXD045323.

Statistics and reproducibility

Age- and weight-matched mice were randomly assigned to the experiments. The number of animals used in each experiment is provided in the respective figure legends. No animals were excluded from the statistical analyses, and the investigators were not blinded during the studies. Except for the animal studies and RNA-seq, which were conducted once, each experiment was repeated at least three times, yielding consistent results. Each experiment included more than three biological replicates. Data are presented as mean ± s.e.m. Group comparisons were performed using a two-tailed unpaired Student's *t*-test or two-way analysis of variance (ANOVA) followed by Tukey's test, as specified in the figure legends. Differences were considered statistically significant at $P < 0.05$. All statistical analyses were processed using OriginLab (v.10.0.0.154), and figures were generated using GraphPad (v.8.0.1).

Reporting summary

Further information on research design is available in the Nature Portfolio Reporting Summary linked to this article.

Data availability

The RNA-seq dataset has been deposited in the NCBI Gene Expression Omnibus database (GSE280845). The mass spectrometry proteomics data have been deposited in the ProteomeXchange database via the PRIDE partner repository, with the dataset identifier PXD045263 and PXD045323. Additional data supporting the findings of this study, including experimental analysis data and statistical information related to the western blot images, are available in the Supplementary Information and/or Source data files. A reporting summary for this article is also available as a Supplementary Information file. Source data are provided with this paper.

References

1. Colberg, S. R. et al. Exercise and type 2 diabetes: the American College of Sports Medicine and the American Diabetes Association joint position statement executive summary. *Diabetes Care* **33**, 2692–2696 (2010).
2. Haskell, W. L. et al. Physical activity and public health: updated recommendation for adults from the American College of Sports Medicine and the American Heart Association. *Circulation* **116**, 1081–1093 (2007).
3. Borst, S. E. Interventions for sarcopenia and muscle weakness in older people. *Age Ageing* **33**, 548–555 (2004).
4. Minuk, H. L. et al. Glucoregulatory and metabolic response to exercise in obese noninsulin-dependent diabetes. *Am. J. Physiol.* **240**, E458–E464 (1981).
5. Hawley, J. A., Hargreaves, M., Joyner, M. J. & Zierath, J. R. Integrative biology of exercise. *Cell* **159**, 738–749 (2014).
6. Murphy, R. M., Watt, M. J. & Febbraio, M. A. Metabolic communication during exercise. *Nat. Metab.* **2**, 805–816 (2020).
7. Egan, B. & Zierath, J. R. Exercise metabolism and the molecular regulation of skeletal muscle adaptation. *Cell Metab.* **17**, 162–184 (2013).
8. Hargreaves, M. & Spriet, L. L. Skeletal muscle energy metabolism during exercise. *Nat. Metab.* **2**, 817–828 (2020).
9. Sylow, L., Kleinert, M., Richter, E. A. & Jensen, T. E. Exercise-stimulated glucose uptake—regulation and implications for glycaemic control. *Nat. Rev. Endocrinol.* **13**, 133–148 (2017).
10. Spaulding, H. R. & Yan, Z. AMPK and the adaptation to exercise. *Annu Rev. Physiol.* **84**, 209–227 (2022).
11. Hoffman, N. J. et al. Global phosphoproteomic analysis of human skeletal muscle reveals a network of exercise-regulated kinases and AMPK substrates. *Cell Metab.* **22**, 922–935 (2015).
12. Gonzalez, A., Hall, M. N., Lin, S. C. & Hardie, D. G. AMPK and TOR: the yin and yang of cellular nutrient sensing and growth control. *Cell Metab.* **31**, 472–492 (2020).

13. Hardie, D. G., Ross, F. A. & Hawley, S. A. AMPK: a nutrient and energy sensor that maintains energy homeostasis. *Nat. Rev. Mol. Cell Biol.* **13**, 251–262 (2012).
14. Herzig, S. & Shaw, R. J. AMPK: guardian of metabolism and mitochondrial homeostasis. *Nat. Rev. Mol. Cell Biol.* **19**, 121–135 (2018).
15. Richter, E. A. & Ruderman, N. B. AMPK and the biochemistry of exercise: implications for human health and disease. *Biochem. J.* **418**, 261–275 (2009).
16. Koh, H. J., Brandauer, J. & Goodyear, L. J. LKB1 and AMPK and the regulation of skeletal muscle metabolism. *Curr. Opin. Clin. Nutr. Metab. Care* **11**, 227–232 (2008).
17. Lim, C. L., Byrne, C. & Lee, J. K. Human thermoregulation and measurement of body temperature in exercise and clinical settings. *Ann. Acad. Med. Singap.* **37**, 347–353 (2008).
18. Nielsen, B. & Nybo, L. Cerebral changes during exercise in the heat. *Sports Med.* **33**, 1–11 (2003).
19. Periard, J. D., Eijsvogels, T. M. H. & Daanen, H. A. M. Exercise under heat stress: thermoregulation, hydration, performance implications, and mitigation strategies. *Physiol. Rev.* **101**, 1873–1979 (2021).
20. Periasamy, M. et al. Role of SERCA pump in muscle thermogenesis and metabolism. *Compr. Physiol.* **7**, 879–890 (2017).
21. Chambers, P. J., Juracic, E. S., Fajardo, V. A. & Tupling, A. R. Role of SERCA and sarcolipin in adaptive muscle remodeling. *Am. J. Physiol. Cell Physiol.* **322**, C382–C394 (2022).
22. Davis, M. et al. Malignant hyperthermia associated with exercise-induced rhabdomyolysis or congenital abnormalities and a novel RYR1 mutation in New Zealand and Australian pedigrees. *Br. J. Anaesth.* **88**, 508–515 (2002).
23. Quane, K. A. et al. Mutation screening of the RYR1 gene in malignant hyperthermia: detection of a novel Tyr to Ser mutation in a pedigree with associated central cores. *Genomics* **23**, 236–239 (1994).
24. Durham, W. J. et al. RyR1 S-nitrosylation underlies environmental heat stroke and sudden death in Y522S RyR1 knockin mice. *Cell* **133**, 53–65 (2008).
25. MacLennan, D. H. $Ca2^{+}$ signalling and muscle disease. *Eur. J. Biochem.* **267**, 5291–5297 (2000).
26. Robinson, R., Carpenter, D., Shaw, M. A., Halsall, J. & Hopkins, P. Mutations in RYR1 in malignant hyperthermia and central core disease. *Hum. Mutat.* **27**, 977–989 (2006).
27. Anderson, D. M. et al. A micropeptide encoded by a putative long noncoding RNA regulates muscle performance. *Cell* **160**, 595–606 (2015).
28. Slack, J. P., Grupp, I. L., Luo, W. & Kranias, E. G. Phospholamban ablation enhances relaxation in the murine soleus. *Am. J. Physiol.* **273**, C1–C6 (1997).
29. Bal, N. C. et al. Sarcolipin is a newly identified regulator of muscle-based thermogenesis in mammals. *Nat. Med.* **18**, 1575–1579 (2012).
30. MacLennan, D. H. & Kranias, E. G. Phospholamban: a crucial regulator of cardiac contractility. *Nat. Rev. Mol. Cell Biol.* **4**, 566–577 (2003).
31. Pant, M., Bal, N. C. & Periasamy, M. Sarcolipin: a key thermogenic and metabolic regulator in skeletal muscle. *Trends Endocrinol. Metab.* **27**, 881–892 (2016).
32. Smith, W. S., Broadbridge, R., East, J. M. & Lee, A. G. Sarcolipin uncouples hydrolysis of ATP from accumulation of Ca2+ by the Ca2+-ATPase of skeletal-muscle sarcoplasmic reticulum. *Biochem. J.* **361**, 277–286 (2002).
33. Chouchani, E. T., Kazak, L. & Spiegelman, B. M. New advances in adaptive thermogenesis: UCP1 and Beyond. *Cell Metab.* **29**, 27–37 (2019).
34. Wolf, G. The uncoupling proteins UCP2 and UCP3 in skeletal muscle. *Nutr. Rev.* **59**, 56–57 (2001).
35. Maurya, S. K. et al. Sarcolipin signaling promotes mitochondrial biogenesis and oxidative metabolism in skeletal muscle. *Cell Rep.* **24**, 2919–2931 (2018).
36. Maurya, S. K. et al. Sarcolipin is a key determinant of the basal metabolic rate, and its overexpression enhances energy expenditure and resistance against diet-induced obesity. *J. Biol. Chem.* **290**, 10840–10849 (2015).
37. Schaffer, B. E. et al. Identification of AMPK Phosphorylation sites reveals a network of proteins involved in cell invasion and facilitates large-scale substrate prediction. *Cell Metab.* **22**, 907–921 (2015).
38. Fentz, J. et al. AMPKα is essential for acute exercise-induced gene responses but not for exercise training-induced adaptations in mouse skeletal muscle. *Am. J. Physiol. Endocrinol. Metab.* **309**, E900–E914 (2015).
39. Fritzen, A. M. et al. 5′-AMP activated protein kinase α2 controls substrate metabolism during post-exercise recovery via regulation of pyruvate dehydrogenase kinase 4. *J. Physiol.* **593**, 4765–4780 (2015).
40. Hingst, J. R. et al. Inducible deletion of skeletal muscle AMPKα reveals that AMPK is required for nucleotide balance but dispensable for muscle glucose uptake and fat oxidation during exercise. *Mol. Metab.* **40**, 101028 (2020).
41. Lantier, L. et al. AMPK controls exercise endurance, mitochondrial oxidative capacity, and skeletal muscle integrity. *FASEB J.* **28**, 3211–3224 (2014).
42. Lee-Young, R. S. et al. Skeletal muscle AMP-activated protein kinase is essential for the metabolic response to exercise in vivo. *J. Biol. Chem.* **284**, 23925–23934 (2009).
43. Narkar, V. A. et al. AMPK and PPARdelta agonists are exercise mimetics. *Cell* **134**, 405–415 (2008).
44. Pinto, A. P. et al. IL-6 deletion decreased REV-ERBα protein and influenced autophagy and mitochondrial markers in the skeletal muscle after acute exercise. *Front. Immunol.* **13**, 953272 (2022).
45. Gatta, L. et al. Modulating the metabolism by trimetazidine enhances myoblast differentiation and promotes myogenesis in cachectic tumor-bearing c26 mice. *Oncotarget* **8**, 113938–113956 (2017).
46. Tupling, A. R., Asahi, M. & MacLennan, D. H. Sarcolipin overexpression in rat slow twitch muscle inhibits sarcoplasmic reticulum Ca2+ uptake and impairs contractile function. *J. Biol. Chem.* **277**, 44740–44746 (2002).
47. Tupling, A. R. et al. Enhanced Ca2+ transport and muscle relaxation in skeletal muscle from sarcolipin-null mice. *Am. J. Physiol. Cell Physiol.* **301**, C841–C849 (2011).
48. Sopariwala, D. H. et al. Sarcolipin overexpression improves muscle energetics and reduces fatigue. *J. Appl Physiol.* **118**, 1050–1058 (2015).
49. Cederberg, A. et al. FOXC2 is a winged helix gene that counteracts obesity, hypertriglyceridemia, and diet-induced insulin resistance. *Cell* **106**, 563–573 (2001).
50. Lidell, M. E. et al. The adipocyte-expressed forkhead transcription factor Foxc2 regulates metabolism through altered mitochondrial function. *Diabetes* **60**, 427–435 (2011).
51. Seo, S. et al. The forkhead transcription factors, Foxc1 and Foxc2, are required for arterial specification and lymphatic sprouting during vascular development. *Dev. Biol.* **294**, 458–470 (2006).
52. Xue, Y. et al. FOXC2 controls Ang-2 expression and modulates angiogenesis, vascular patterning, remodeling, and functions in adipose tissue. *Proc. Natl Acad. Sci. USA* **105**, 10167–10172 (2008).
53. Gozo, M. C. et al. Foxc2 induces Wnt4 and Bmp4 expression during muscle regeneration and osteogenesis. *Cell Death Differ.* **20**, 1031–1042 (2013).

54. Mu, J., Brozinick, J. T. Jr., Valladares, O., Bucan, M. & Birnbaum, M. J. A role for AMP-activated protein kinase in contraction- and hypoxia-regulated glucose transport in skeletal muscle. *Mol. Cell* **7**, 1085–1094 (2001).
55. Fujii, N. et al. AMP-activated protein kinase α2 activity is not essential for contraction- and hyperosmolarity-induced glucose transport in skeletal muscle. *J. Biol. Chem.* **280**, 39033–39041 (2005).
56. Maarbjerg, S. J. et al. Genetic impairment of AMPKα2 signaling does not reduce muscle glucose uptake during treadmill exercise in mice. *Am. J. Physiol. Endocrinol. Metab.* **297**, E924–E934 (2009).
57. Merry, T. L., Steinberg, G. R., Lynch, G. S. & McConell, G. K. Skeletal muscle glucose uptake during contraction is regulated by nitric oxide and ROS independently of AMPK. *Am. J. Physiol. Endocrinol. Metab.* **298**, E577–E585 (2010).
58. Liu, X. et al. Activation of GPR81 by lactate drives tumour-induced cachexia. *Nat. Metab.* **6**, 708–723 (2024).
59. Xiao, L. et al. AMPK-dependent and -independent coordination of mitochondrial function and muscle fiber type by FNIP1. *PLoS Genet.* **17**, e1009488 (2021).
60. Hu, X. et al. A gut-derived hormone regulates cholesterol metabolism. *Cell* **187**, 1685–1700.e18 (2024).
61. Castro, B. & Kuang, S. Evaluation of muscle performance in mice by treadmill exhaustion test and whole-limb grip strength assay. *Bio-Protoc.* **7**, e2237 (2017).
62. Han, J. et al. The CREB coactivator CRTC2 controls hepatic lipid metabolism by regulating SREBP1. *Nature* **524**, 243–246 (2015).
63. Kim, D., Langmead, B. & Salzberg, S. L. HISAT: a fast spliced aligner with low memory requirements. *Nat. Methods* **12**, 357–360 (2015).
64. Love, M. I., Huber, W. & Anders, S. Moderated estimation of fold change and dispersion for RNA-seq data with DESeq2. *Genome Biol.* **15**, 550 (2014).
65. Wu, T. et al. clusterProfiler 4.0: a universal enrichment tool for interpreting omics data. *Innovation* **2**, 100141 (2021).
66. Tabebordbar, M. et al. Directed evolution of a family of AAV capsid variants enabling potent muscle-directed gene delivery across species. *Cell* **184**, 4919–4938.e4922 (2021).

Acknowledgements

We thank H. Deng, S.-C. Lin and all laboratory members for discussion and technical help. We thank I. Hanson for editing. This work was supported by grants from the Ministry of Science and Technology of the People's Republic of China (2021YFA0804801), the National Natural Science Foundation of China (82088102, 31830040 and 91957206), Dushi Program and Pillars of the Nation Funding for Life Sciences, Tsinghua University to Y.W.

Author contributions

Y.P., L.J., X.H., X.S. and X.F. performed the experiments. Y.Q. and Z.G. provided critical materials. Y.W. conceived, designed and supervised the study. Y.W., Y.P. and L.J. wrote the paper. All authors reviewed and commented on the paper.

Competing interests

The authors declare no competing interests.

Additional information

Extended data is available for this paper at https://doi.org/10.1038/s42255-024-01176-8.

Supplementary information The online version contains supplementary material available at https://doi.org/10.1038/s42255-024-01176-8.

Correspondence and requests for materials should be addressed to Yiguo Wang.

Peer review information *Nature Metabolism* thanks Muthu Periasamy and the other, anonymous, reviewer(s) for their contribution to the peer review of this work. Primary Handling Editor: Revati Dewal, in collaboration with the *Nature Metabolism* team.

https://doi.org/10.1038/s42255-024-01176-8

a

	fl/fl	*cFeimin* MKO
Body weight (g)	29.70 ± 0.67	28.48 ± 1.17
Fat mass (%)	11.23 ± 0.91	10.84 ± 0.90
Lean mass (%)	83.57 ± 0.98	83.70 ± 0.88
Liver(g)	1.257 ± 0.049	1.119 ± 0.076
BAT (g)	0.114 ± 0.007	0.106 ± 0.008
Epididymal WAT (g)	0.526 ± 0.036	0.517 ± 0.042
Gas (g)	0.345 ± 0.006	0.338 ± 0.013
Sol (g)	0.020 ± 0.001	0.018 ± 0.001
TA (g)	0.115 ± 0.003	0.111 ± 0.004
Heart (g)	0.170 ± 0.010	0.158 ± 0.009

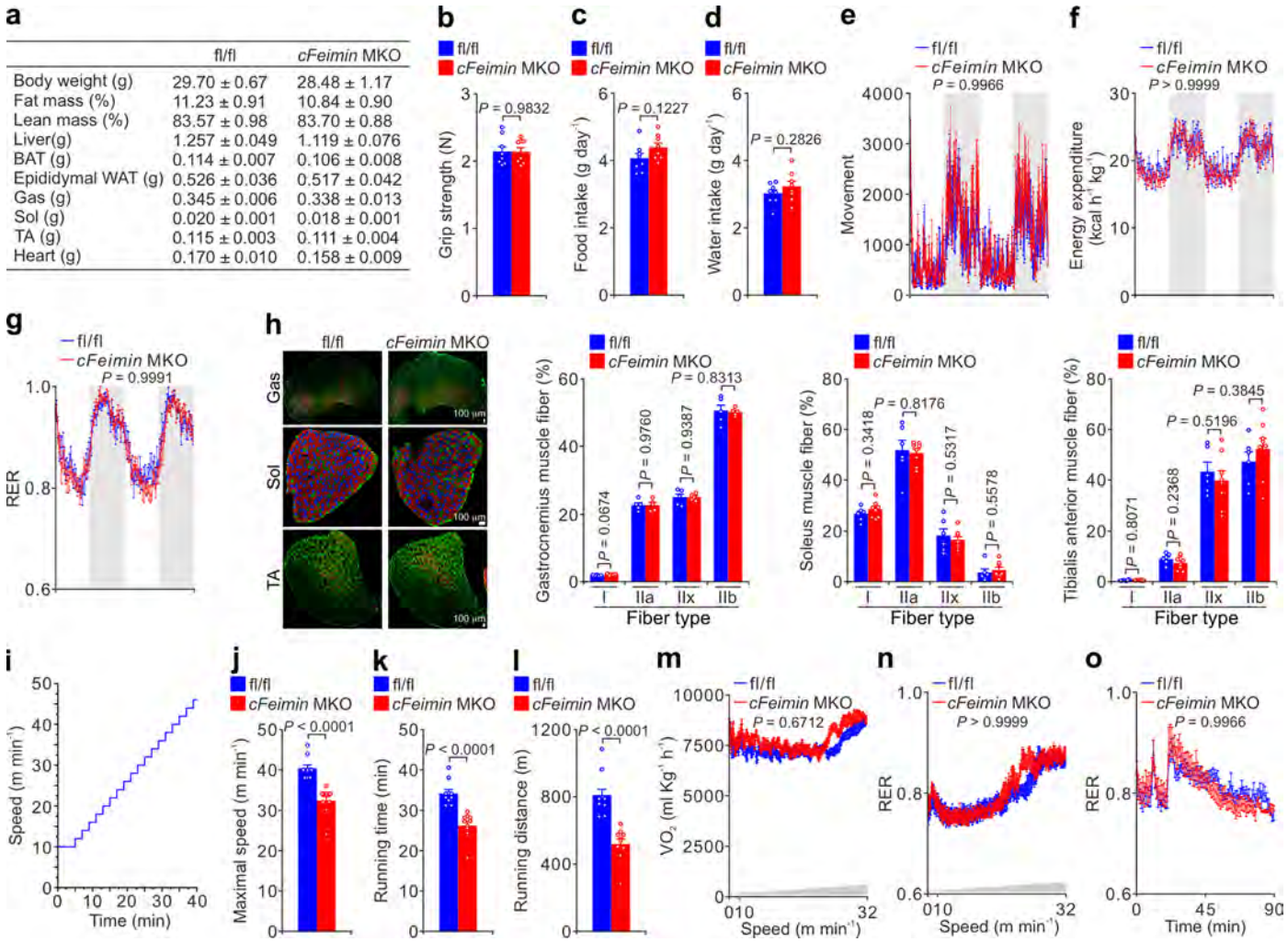

Extended Data Fig. 1 | Loss of *cFeimin* does not affect skeletal muscle development and fibre type reprograming. a-g, Body and tissue weight (**a**), grip strength (**b**), food intake (**c**), water intake (**d**), movement (**e**), energy expenditure (**f**) and respiratory exchange ratio (RER, **g**) were assessed in 10-week-old male wild-type (fl/fl) and *cFeimin* MKO mice. n = 8 mice. **h**, Fibre type staining and quantification were performed in male fl/fl and *cFeimin* MKO mice. n = 5-8 mice. **i**, A schematic diagram illustrating the time course of acute treadmill running. **j-l**, The maximal running speed (**j**), running time (**k**) and running distance (**l**) were measured in 10-week-old male fl/fl and *cFeimin* MKO mice. n = 10 mice. m-n, VO_2 (**m**) and RER (**n**) were assessed in male fl/fl and *cFeimin* MKO mice under high-intensity exercise. n = 8 mice. **o**, RER was evaluated in male fl/fl and *cFeimin* MKO mice during low-intensity exercise. n = 8 mice. Data are shown as mean ± s.e.m. Statistical comparisons were performed using an unpaired two-tailed Student's *t*-test (**b-d, h, j-l**) or two-way ANOVA followed by Tukey's test (**e-g, m-o**). All individual points and *P* values are shown.

https://doi.org/10.1038/s42255-024-01176-8

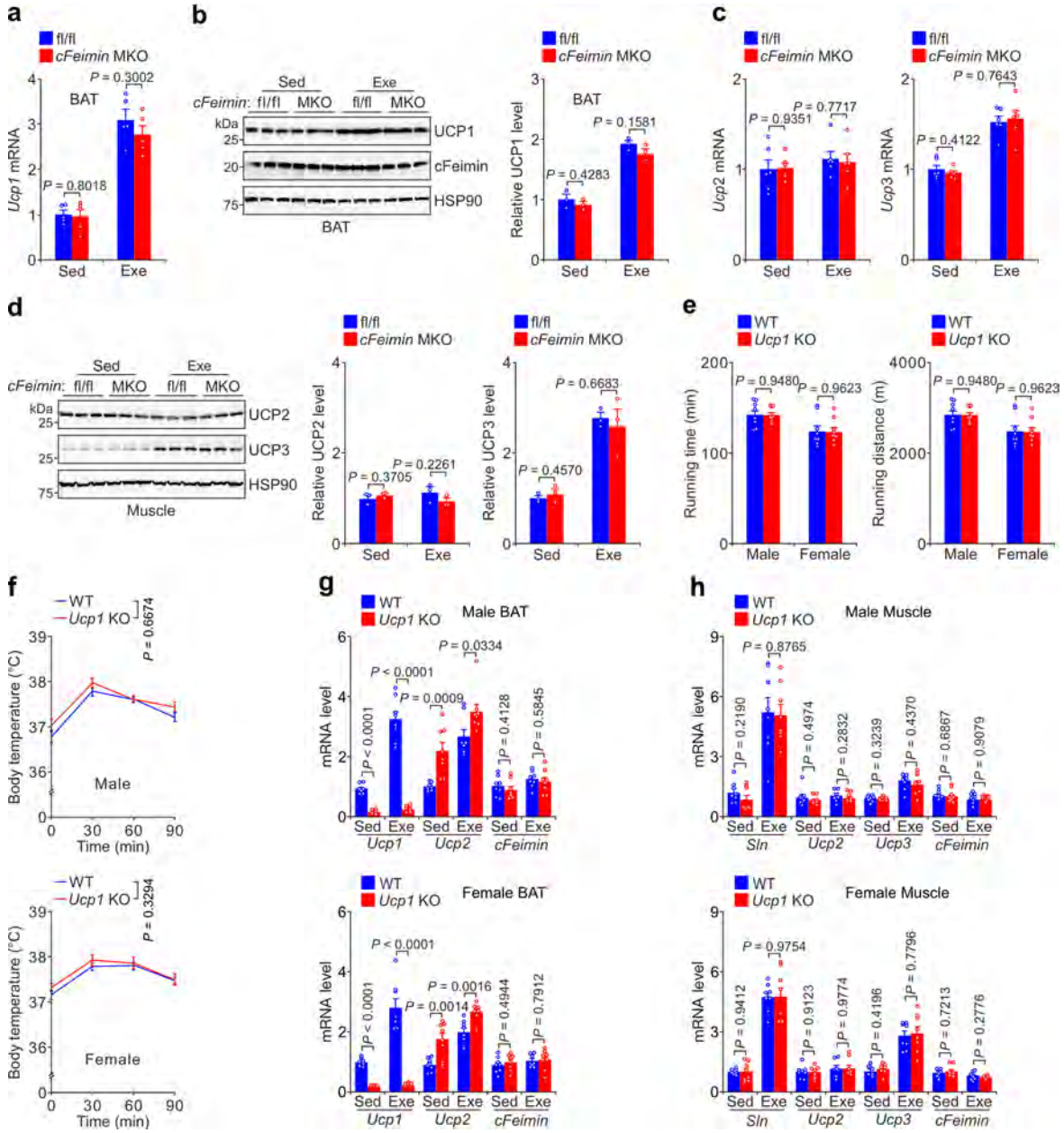

Extended Data Fig. 2 | *cFeimin* deficiency does not affect the expression of uncoupling proteins. a-b, qPCR results (**a**) and immunoblots (**b**) showing the expression of UCP1 in brown adipose tissue (BAT) extracts of 10-week-old male fl/fl and *cFeimin* MKO mice. n = 5 mice (a), n = 3 biological replicates (b). **c-d**, qPCR results (**c**) and immunoblots (**d**) showing the expression of UCP2 and UCP3 in gastrocnemius muscle tissue extracts of male fl/fl and *cFeimin* MKO mice. n = 6 mice (c), n = 3 biological replicates (d). **e**, Running time and running distance of 10-week-old male and female wild-type (WT) and *Ucp1* KO mice. n = 8 mice. **f**, Rectal temperature of male and female WT and *Ucp1* KO mice was monitored during exercise. n = 8 mice. **g**. qPCR showing *Ucp1*, *Ucp2* and *cFeimin* expression in BAT extracts from WT and *Ucp1* KO mice under sedentary conditions (Sed) or after 90 minutes of exercise (Exe). n = 8 mice. **h**. qPCR showing *cFeimin*, *Sln*, *Ucp2* and *Ucp3* expression in gastrocnemius muscle extracts from WT and *Ucp1* KO mice under sedentary conditions (Sed) or after 90 minutes of exercise (Exe). n = 8 mice. Data are shown as mean ± s.e.m. Statistical comparisons were performed using an unpaired two-tailed Student's *t*-test (**a-e, g, h**) or two-way ANOVA followed by Tukey's test (**f**). All individual points and *P* values are shown.

https://doi.org/10.1038/s42255-024-01176-8

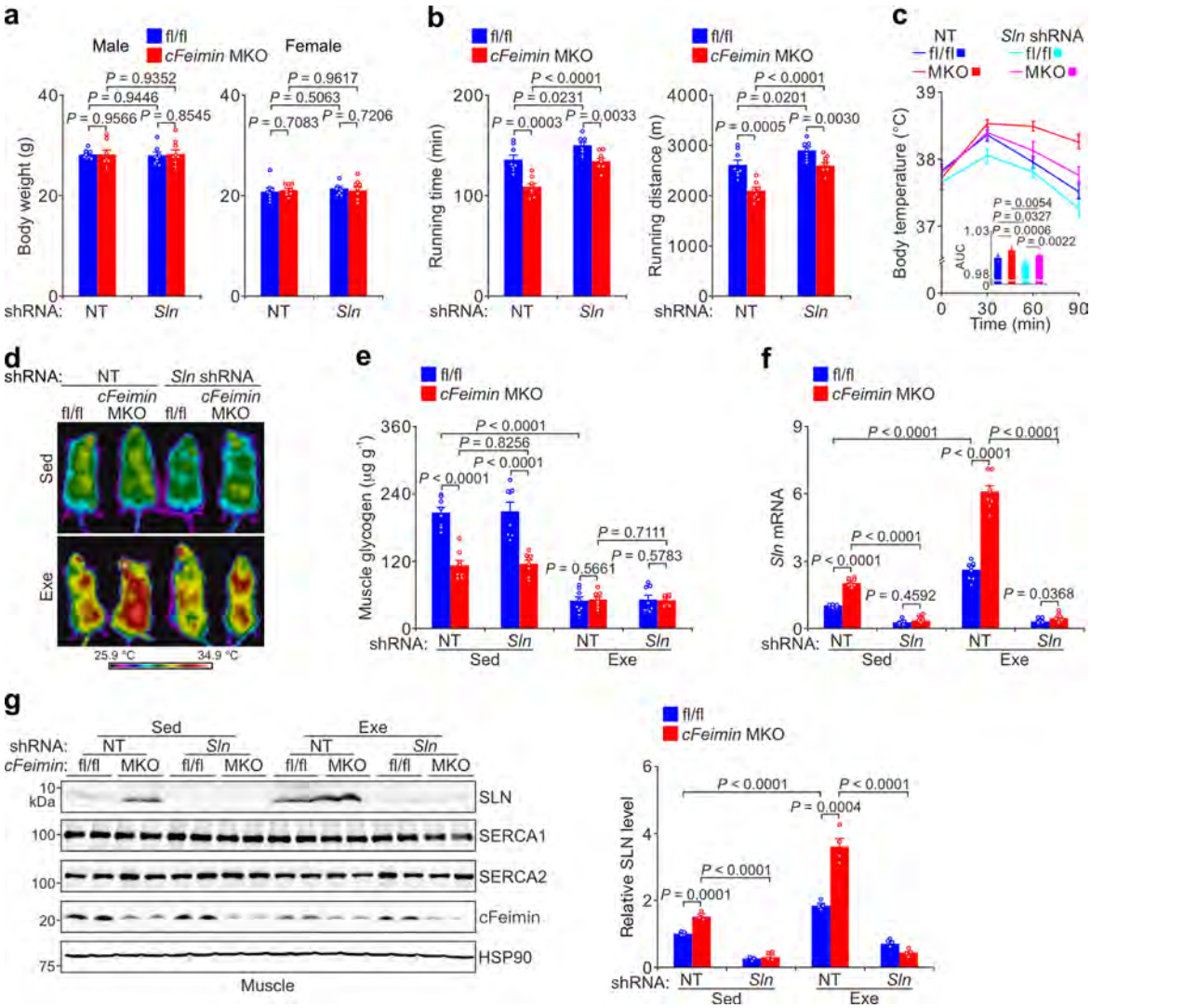

Extended Data Fig. 3 | cFeimin regulates exercise capacity through SLN in female mice. a, Body weight was assessed in 10-week-old wild-type (fl/fl) and *cFeimin* MKO mice after injection of myoAAV-con or myoAAV-sh*Sln* for 1.5 months. n = 8 mice. **b**, Running time and running distance of 10-week-old female fl/fl and *cFeimin* MKO mice with or without *Sln* knockdown by shRNA. n = 8 mice. NT, non-targeting shRNA. **c-d**, Rectal temperature (**c**) and body surface temperature (**d**) were monitored during exercise in female fl/fl and *cFeimin* MKO mice with or without *Sln* shRNA knockdown. n = 8 mice (c). **e**, Muscle glycogen levels in female fl/fl and *cFeimin* MKO mice with or without *Sln* shRNA knockdown before exercise (sedentary (Sed)) or after 90 minutes of exercise (Exe). n = 8 mice. **f-g**, qPCR (**f**), and immunoblots and statistical data (**g**) showing SLN expression in gastrocnemius muscle extracts from female fl/fl and *cFeimin* MKO mice with or without *Sln* shRNA knockdown under sedentary conditions (Sed) or after 90 minutes of exercise (Exe). n = 8 mice (f), n = 4 biological replicates (g). Data are shown as mean ± s.e.m. Statistical comparisons were performed using two-way ANOVA followed by Tukey's test (**a-c, e-g**). All individual points and *P* values are shown.

https://doi.org/10.1038/s42255-024-01176-8

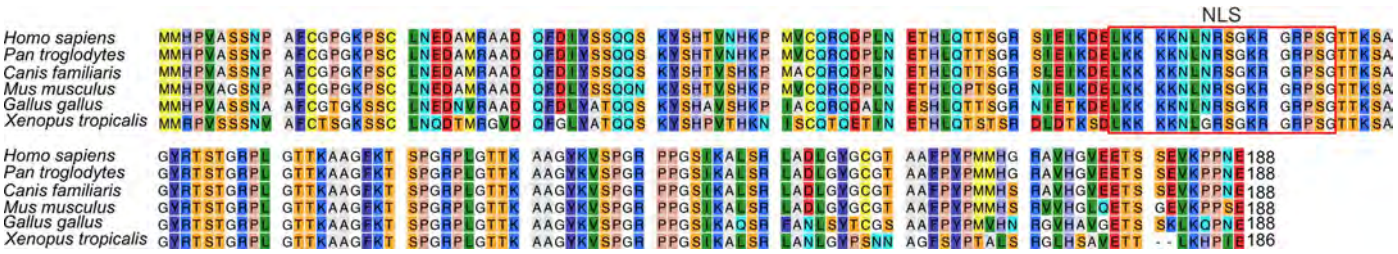

Extended Data Fig. 4 | Alignment of the amino acid sequence of cFeimin from different species. The nuclear localization signal (NLS) is indicated by the red box.

https://doi.org/10.1038/s42255-024-01176-8

a

	fl/fl	*Foxc2* MKO
Body weight (g)	29.95 ± 0.86	28.80 ± 0.68
Fat mass (%)	10.65 ± 0.96	11.33 ± 0.99
Lean mass (%)	84.80 ± 1.34	84.76 ± 1.00
Liver(g)	1.288 ± 0.051	1.259 ± 0.021
BAT (g)	0.122 ± 0.005	0.140 ± 0.008
Epididymal WAT (g)	0.721 ± 0.084	0.650 ± 0.060
Gas (g)	0.344 ± 0.009	0.344 ± 0.005
Sol (g)	0.018 ± 0.001	0.021 ± 0.001
TA (g)	0.106 ± 0.003	0.105 ± 0.002
Heart (g)	0.168 ± 0.009	0.168 ± 0.014

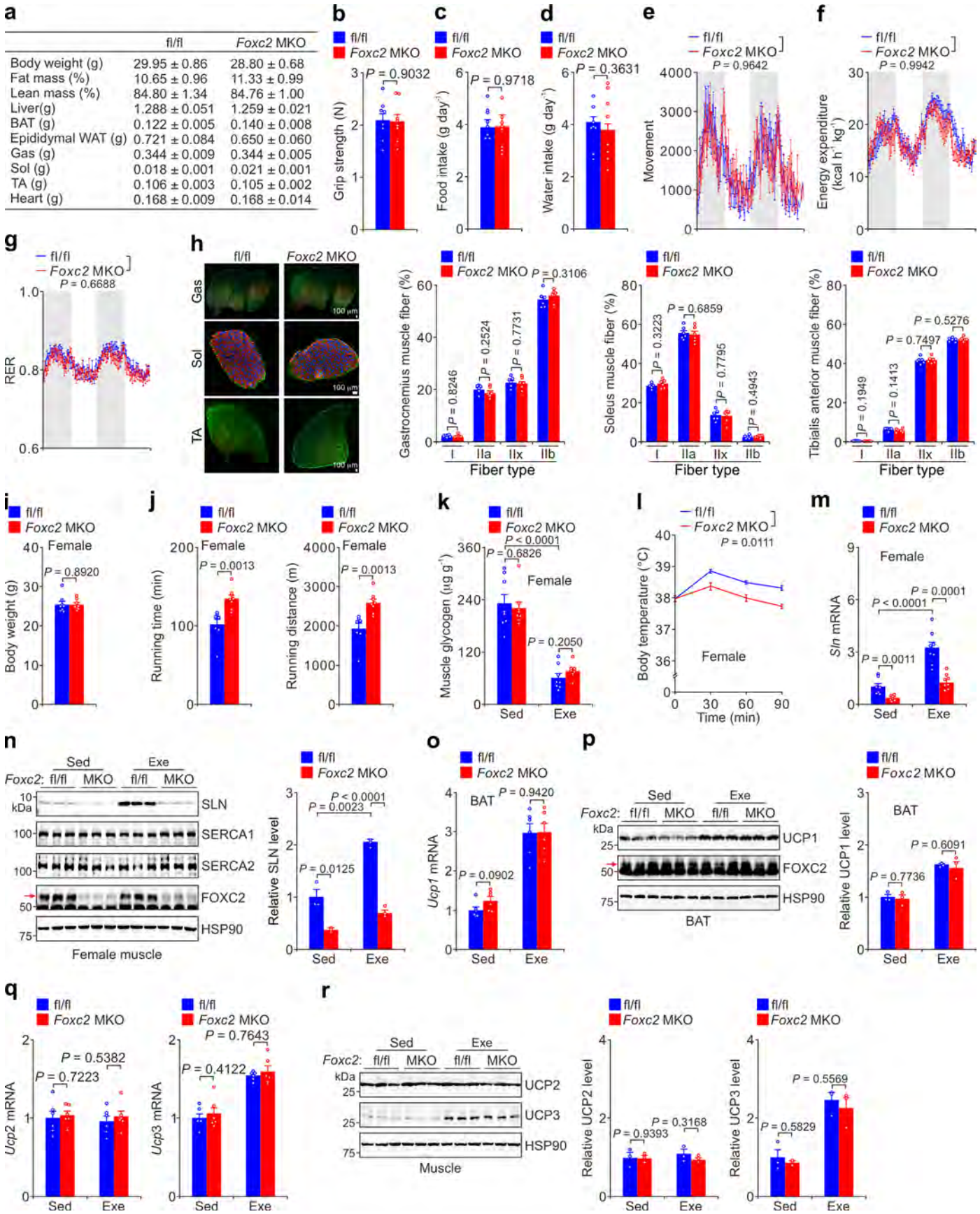

Extended Data Fig. 5 | See next page for caption.

https://doi.org/10.1038/s42255-024-01176-8

Extended Data Fig. 5 | Deletion of *Foxc2* in skeletal muscle increases muscle exercise capacity and does not affect skeletal muscle development. **a-g**, Measurements of body and tissue weight (**a**), grip strength (**b**), food intake (**c**), water intake (**d**), movement (**e**), energy expenditure (**f**) and respiratory exchange ratio (RER, **g**) in 10-week-old male wild-type (fl/fl) and *Foxc2* MKO mice. n = 8 mice. **h**, Staining and quantification of fibre types in male fl/fl and *Foxc2* MKO mice. n = 6 mice. **i**, Body weight was assessed in 10-week-old female wild-type (fl/fl) and *Foxc2* MKO mice. n = 8 mice. **j**, Running time and running distance of 10-week-old female wild-type (fl/fl) and *Foxc2* MKO mice. n = 8 mice. **k**, Muscle glycogen levels in female WT and *Foxc2* MKO mice before exercise (sedentary (Sed)) or after 90 minutes of exercise (Exe). n = 8 mice. **l**, Rectal temperature of female wild-type (fl/fl) and *Foxc2* MKO mice was monitored during exercise. n = 8 mice. **m-n**, qPCR (**m**) and immunoblots (**n**) showing SLN expression in gastrocnemius muscle extracts from female WT and *Foxc2* MKO mice under sedentary conditions (Sed) or after 90 minutes of exercise (Exe). n = 8 mice (m), n = 3 biological replicates (n). **o-p**, qPCR results (**o**) and immunoblots (**p**) showing the expression of UCP1 in brown adipose tissue (BAT) extracts of fl/fl and *Foxc2* 10-week-old male MKO mice. On the immunoblot, FOXC2 is denoted by the red arrow. n = 6 mice (**o**), n = 3 biological replicates (**p**). **q-r**, qPCR results (**q**) and immunoblots (**r**) showing the expression of UCP2 and UCP3 in gastrocnemius muscle tissue extracts from male fl/fl and *Foxc2* MKO mice. n = 6 mice (q), n = 3 biological replicates (r). Data are shown as mean ± s.e.m. Statistical comparisons were performed using an unpaired two-tailed Student's *t*-test (**b-d, h-j, o-r**) or two-way ANOVA followed by Tukey's test (**e**–**g**,**k**–**n**). All individual points and *P* values are shown.

https://doi.org/10.1038/s42255-024-01176-8

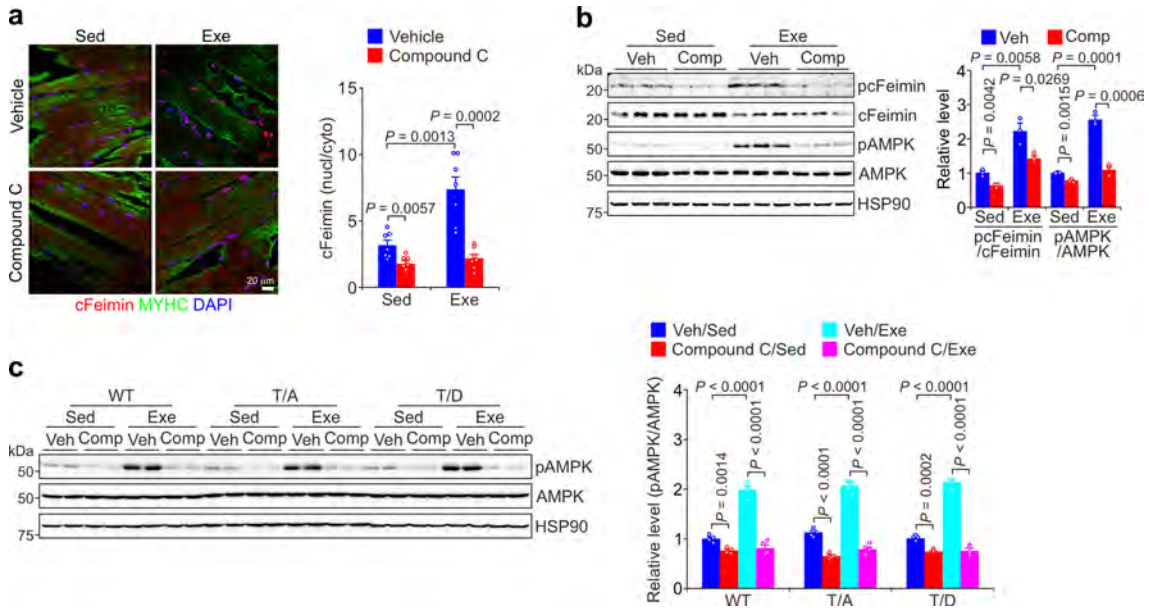

Extended Data Fig. 6 | AMPK phosphorylates cFeimin and promotes its nuclear translocation in female mice. a, The AMPK inhibitor Compound C (8 mg/kg) effectively prevents the exercise-induced nuclear translocation of cFeimin. n = 7 female mice. Mice were analysed 24 hr after injection of Compound C or PBS (Veh). **b**, Immunoblots show the phosphorylation of cFeimin in gastrocnemius muscle extracts from sedentary (Sed) and exercised (Exe) female mice injected with PBS (Veh) or Compound C (Comp, 8 mg/kg). 24 hrs after injection, mice were subjected to 90-minute exercise or not, then analysed. n = 3 biological replicates. **c**, Immunoblots (left panel) and statistical data (right panel) demonstrate the phosphorylation of AMPK in gastrocnemius muscle extracts from male mice injected with PBS (Veh) or Compound C (Comp, 8 mg/kg for 24 hrs) under sedentary (Sed) or 90-minute exercise (Exe) conditions. n = 4 biological replicates. Data are shown as mean ± s.e.m. Statistical comparisons were performed using two-way ANOVA followed by Tukey's test (**a**-**c**). All individual points and *P* values are shown.

https://doi.org/10.1038/s42255-024-01176-8

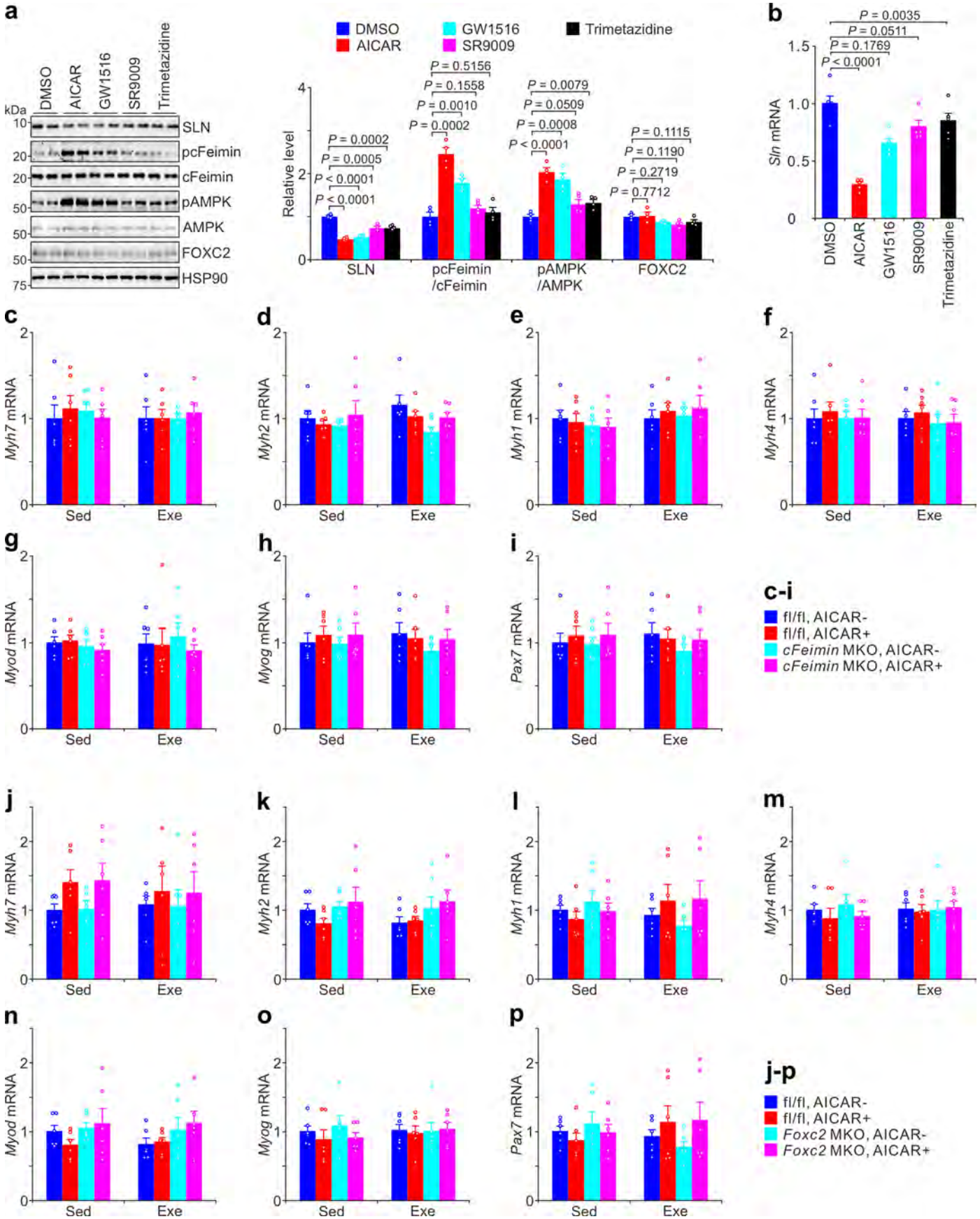

Extended Data Fig. 7 | See next page for caption.

https://doi.org/10.1038/s42255-024-01176-8

Extended Data Fig. 7 | Short-term AICAR treatment has no effect on muscle development and fibre type reprograming. a-b, Immunoblots and statistical data (**a**), and qPCR results (**b**) showing the effect of AMPK-activated doping on SLN expression in myotubes. Myotubes were treated by AICAR (1 mM), GW1516 (100 nM), SR9009 (10 μM) and Trimetazidine (150 μM) for 3 hrs. n = 4 biological replicates (a), n = 5 biological replicates (b). **c-i**, qPCR results demonstrate the expression of fibre type genes (**c-f**) and myogenesis genes (**g-i**) in 10-week-old male fl/fl and *cFeimin* MKO mice with or without AICAR treatment. Mice were intraperitoneally injected with AICAR (500 mg/kg/day) for 2 weeks. n = 6 mice. **j-p**, qPCR results illustrate the expression of fibre type genes (**j-m**) and myogenesis genes (**n-p**) in 10-week-old male fl/fl and *Foxc2* MKO mice with or without AICAR treatment. Mice were intraperitoneally injected with AICAR (500 mg/kg/day) for 2 weeks. n = 6 mice. Data are shown as mean ± s.e.m. Statistical comparisons were performed using two-way ANOVA followed by Tukey's test. All individual points and *P* values are shown.

nature portfolio

Corresponding author(s): Yiguo WANG

Last updated by author(s): Nov 1, 2024

Reporting Summary

Nature Portfolio wishes to improve the reproducibility of the work that we publish. This form provides structure for consistency and transparency in reporting. For further information on Nature Portfolio policies, see our Editorial Policies and the Editorial Policy Checklist.

Statistics

For all statistical analyses, confirm that the following items are present in the figure legend, table legend, main text, or Methods section.

n/a	Confirmed	
☐	☒	The exact sample size (*n*) for each experimental group/condition, given as a discrete number and unit of measurement
☐	☒	A statement on whether measurements were taken from distinct samples or whether the same sample was measured repeatedly
☐	☒	The statistical test(s) used AND whether they are one- or two-sided *Only common tests should be described solely by name; describe more complex techniques in the Methods section.*
☒	☐	A description of all covariates tested
☒	☐	A description of any assumptions or corrections, such as tests of normality and adjustment for multiple comparisons
☐	☒	A full description of the statistical parameters including central tendency (e.g. means) or other basic estimates (e.g. regression coefficient) AND variation (e.g. standard deviation) or associated estimates of uncertainty (e.g. confidence intervals)
☐	☒	For null hypothesis testing, the test statistic (e.g. *F*, *t*, *r*) with confidence intervals, effect sizes, degrees of freedom and *P* value noted *Give P values as exact values whenever suitable.*
☒	☐	For Bayesian analysis, information on the choice of priors and Markov chain Monte Carlo settings
☒	☐	For hierarchical and complex designs, identification of the appropriate level for tests and full reporting of outcomes
☒	☐	Estimates of effect sizes (e.g. Cohen's *d*, Pearson's *r*), indicating how they were calculated

Our web collection on statistics for biologists contains articles on many of the points above.

Software and code

Policy information about availability of computer code

Data collection	ZEN 2011 was used to collect data from Zeiss780 confocal microscopy. Thermo Fisher Scientific Proteome Discover and XcaliburTM were used to collect data from mass spectrometry. Calcium images were collected and analyzed using the MetaFluor software(v.7.10.4.407) package from Molecular Devices.
Data analysis	Software and packages used in RNASeq data analysis is described below: Quality assessment was processed using FastQC tool (v.0.12.1) and SOAPnuke (v.1.5.2); Genome alignment was processed using HISAT2 (v.2.2.1); BAM files sorting was processed using SAMtools (v.1.9); Post-alignment quality control was processed using SAMstat(v 1.5.2). Reads counting was processed using StringTie (v.2.1.4); RNASeq Secondary statistical analysis was processed using R (v.4.3); Differential gene expression analysis was processed using DESeq2 (v.1.40.2); Gene ontology enrichment analysis was processed using clusterProfiler (v.4.7.1); Principal-component analysis was processed using PCATools (v.2.14.0). Statistical analysis was performed using OriginLab (v.10.0.0.154) and GraphPad (v.8.0.1). The level and distribution of cellular fluorescence from fluorescence microscopy images was determined using ImageJ (v.1.54).

For manuscripts utilizing custom algorithms or software that are central to the research but not yet described in published literature, software must be made available to editors and reviewers. We strongly encourage code deposition in a community repository (e.g. GitHub). See the Nature Portfolio guidelines for submitting code & software for further information.

Data

Policy information about availability of data

All manuscripts must include a data availability statement. This statement should provide the following information, where applicable:

- Accession codes, unique identifiers, or web links for publicly available datasets
- A description of any restrictions on data availability
- For clinical datasets or third party data, please ensure that the statement adheres to our policy

Raw and processed RNA-seq datasets are uploaded and available in NCBI's GEO database under the accession number (GSE280845).
The mass spectrometry proteomics data have been deposited to ProteomeXchange database through the PRIDE partner repository, with the dataset identifier PXD045263 and PXD045323.
Additional data supporting the findings of this study, including experimental analysis data and statistical information related to the Western blot images, are available in the Supplementary Information and/or Source Data file. A reporting summary for this article is also available as a Supplementary Information file.

Research involving human participants, their data, or biological material

Policy information about studies with human participants or human data. See also policy information about sex, gender (identity/presentation), and sexual orientation and race, ethnicity and racism.

Reporting on sex and gender	N/A
Reporting on race, ethnicity, or other socially relevant groupings	N/A
Population characteristics	N/A
Recruitment	N/A
Ethics oversight	N/A

Note that full information on the approval of the study protocol must also be provided in the manuscript.

Field-specific reporting

Please select the one below that is the best fit for your research. If you are not sure, read the appropriate sections before making your selection.

☒ Life sciences ☐ Behavioural & social sciences ☐ Ecological, evolutionary & environmental sciences

For a reference copy of the document with all sections, see nature.com/documents/nr-reporting-summary-flat.pdf

Life sciences study design

All studies must disclose on these points even when the disclosure is negative.

Sample size	In both in vitro and in vivo investigations, the sample size was determined based on the prior experience of our laboratory and the available literature and protocols. We set a minimum of four animals per group to enable essential statistical analysis. In vitro experiments utilizing cultured cells were performed at least three times to guarantee reproducibility. Detailed information regarding all sample sizes can be found in the corresponding figure legends.
Data exclusions	No animal data was excluded from the analyses.
Replication	For all experiments we used multiple biological replicates, as indicated in the figure legends. For quantitative measurements, three or more independent experiments were carried out and statistical analysis performed.
Randomization	Samples were randomly assigned for the experiments.
Blinding	The investigators were not blinded in the studies, as they needed to know the group assignments to perform the assays.

Reporting for specific materials, systems and methods

We require information from authors about some types of materials, experimental systems and methods used in many studies. Here, indicate whether each material, system or method listed is relevant to your study. If you are not sure if a list item applies to your research, read the appropriate section before selecting a response.

Materials & experimental systems

n/a	Involved in the study
☐	☒ Antibodies
☐	☒ Eukaryotic cell lines
☒	☐ Palaeontology and archaeology
☐	☒ Animals and other organisms
☒	☐ Clinical data
☒	☐ Dual use research of concern
☒	☐ Plants

Methods

n/a	Involved in the study
☒	☐ ChIP-seq
☒	☐ Flow cytometry
☒	☐ MRI-based neuroimaging

Antibodies

Antibodies used

All antibodies used for western blotting, immunofluorescence and chromatin immunoprecipitation are provided as follows:
Western blot:
anti-Feimin (PA5-66500, 1:1000, Invitrogen)
anti-AMPKα (2532, 1:1000, Cell Signaling Technology)
anti-pAMPKα (2535, 1:1000, Cell Signaling Technology)
anti-HSP90 (4874S, 1:1000, Cell Signaling Technology)
anti-UCP1 (14670, 1:1000, Cell Signaling Technology)
anti-SERCA1a (22361, 1:1000, Proteintech)
anti-SERCA2a (67248, 1:1000, Proteintech)
anti-UCP2 (11081-1, 1:1000, Proteintech)
anti-UCP3 (A1532, 1:1000, ABclonal)
anti-SLN (ABT13, 1:1000, Sigma-Aldrich)
anti-FOXC2 (sc-515234, 1:1000, Santa Cruz)
anti-rabbit polyclonal anti-pcFeimin antibody (1:1000, generated and purified by ABclonal)
Goat anti-mouse IgG(H+L)-HRP conjugate (1706516,1:5000, BIO-RAD)
Goat anti-Rabbit IgG(H+L)-HRP conjugate (1706515,1:5000, BIO-RAD)
Immunofluorescence:
anti-Flag (F1804, 1:1000, Sigma-Aldrich);
anti-MYHI (BA-D5s,1:200, DHSB);
anti-MYHIIa (SC-71, 1:200, DHSB);
anti-MYHIIX (6H1, 1:200, DHSB);
anti-MYHC (MF 20, 1:200, DHSB),
anti-dystrophin (ab15277,1:1000, Abcam)
anti-cFeimin (1:1000, generated and purified by ABclonal)
Goat anti-Mouse IgG1, Alexa Fluor 568 (A-21124,1:1000, Thermo Fisher Scientific)
Goat anti-Mouse IgG2b, Alexa Fluor 647 (A-21242,1:1000, Thermo Fisher Scientific)
Goat anti-Mouse IgM, Alexa Fluor 488 (A-21042,1:1000, Thermo Fisher Scientific)
Goat anti-Mouse , Alexa Fluor 546 (A-11003,1:1000, Thermo Fisher Scientific)
Donkey anti-Rabbit , Alexa Fluor 488 (A21206,1:1000, Thermo Fisher Scientific)
Donkey anti-Rabbit IgG, Alexa Fluor 555 (A-32816,1:1000, Thermo Fisher Scientific)
immunoprecipitation:
anti-flag-hrp (AE024, 1:1000, ABclonal)
anti-HA (561, 1:1000, MBL)

Validation

All antibodies used in this study were commercially developed.
anti-Feimin was validated for immunofluorescent staining in human cell line SiHa, https://www.thermofisher.cn/cn/zh/antibody/product/C5orf24-Antibody-Polyclonal/PA5-66500.
anti-AMPKα was validated for WB in various cell lines, https://www.cellsignal.com/products/primary-antibodies/ampka-antibody/2532.
anti-pAMPKα was validated for WB in various cell lines, https://www.cellsignal.com/product/productDetail.jsp?productId=2535.
anti-HSP90 was validated for WB in various cell lines, https://www.cellsignal.com/product/productDetail.jsp?productId=4874.
anti-UCP1 was validated for WB in various cell lines, https://www.cellsignal.com/product/productDetail.jsp?productId=14670.
anti-SERCA1a was validated for WB in various cell lines, https://www.ptgcn.com/Products/ATP2A1-Antibody-22361-1-AP.htm.
anti-SERCA2a was validated for FC in HeLa cells, https://www.ptgcn.com/products/SERCA2-ATP2A2-Antibody-CL488-67248.htm.
anti-UCP2 was validated for WB in various cell lines, https://www.ptgcn.com/products/UCP2-Antibody-11081-1-AP.htm.
anti-UCP3 was validated for WB in various cell lines, https://abclonal.com.cn/catalog/A1532.
anti-SLN was validated for WB in various cell lines, https://www.sigmaaldrich.cn/CN/zh/product/mm/abt13.
anti-FOXC2 was validated for WB in various cell lines, https://www.scbt.com/p/foxc2-antibody-g-7.
anti-rabbit polyclonal anti-pcFeimin antibody was validated for WB in our figure 6e and s6b.
anti-Flag was validated for WB, immunoprecipitation and immunofluorescence in various cell lines, https://www.sigmaaldrich.cn/CN/zh/product/sigma/f1804.
anti-MYHI was validated for immunofluorescence in skeletal muscle, https://dshb.biology.uiowa.edu/BA-D5.
anti-MYHIIa was validated for immunofluorescence in skeletal muscle, https://dshb.biology.uiowa.edu/SC-71.
anti-MYHIIX was validated for immunofluorescence in skeletal muscle, https://dshb.biology.uiowa.edu/6H1.
anti-MYHC was validated for immunofluorescence in skeletal muscle, https://dshb.biology.uiowa.edu/MF-20.
anti-Dystrophin was validated for immunofluorescence in skeletal muscle, https://www.abcam.com/products/primary-antibodies/dystrophin-antibody-ab15277.html.
anti-cFeimin was validated for immunofluorescence in our WT and global KO mice skeletal muscle.

Goat anti-Mouse IgG1, Alexa Fluor 568 was validated for immunofluorescence in different tissues and cells, https://www.thermofisher.cn/cn/zh/antibody/product/Goat-anti-Mouse-IgG1-Cross-Adsorbed-Secondary-Antibody-Polyclonal/A-21124.
Goat anti-Mouse IgG2b, Alexa Fluor 647 was validated for immunofluorescence in different tissues and cells, https://www.thermofisher.cn/cn/zh/antibody/product/Goat-anti-Mouse-IgG2b-Cross-Adsorbed-Secondary-Antibody-Polyclonal/A-21242.
Goat anti-Mouse IgM, Alexa Fluor 488 was validated for immunofluorescence in different tissues and cells, https://www.thermofisher.cn/cn/zh/antibody/product/Goat-anti-Mouse-IgM-Heavy-chain-Cross-Adsorbed-Secondary-Antibody-Polyclonal/A-21042.
Goat anti-Mouse , Alexa Fluor 546 was validated for immunofluorescence in different tissues and cells, https://www.thermofisher.cn/cn/zh/antibody/product/Goat-anti-Mouse-IgG-H-L-Cross-Adsorbed-Secondary-Antibody-Polyclonal/A-11003.
Donkey anti-Rabbit , Alexa Fluor 488 was validated for immunofluorescence in different tissues and cells, https://www.thermofisher.cn/cn/zh/antibody/product/Donkey-anti-Rabbit-IgG-H-L-Highly-Cross-Adsorbed-Secondary-Antibody-Polyclonal/A-21206.
Donkey anti-Rabbit IgG, Alexa Fluor 555 was validated for immunofluorescence in different tissues and cells, https://www.thermofisher.cn/cn/zh/antibody/product/Donkey-anti-Goat-IgG-H-L-Highly-Cross-Adsorbed-Secondary-Antibody-Polyclonal/A32816.
anti-flag-hrp was validated for WB in various cell lines, https://abclonal.com.cn/catalog/AE024.
anti-HA was validated for WB in various cell lines, https://www.mblbio.com/bio/g/dtl/A/?pcd=561.

Eukaryotic cell lines

Policy information about cell lines and Sex and Gender in Research

Cell line source(s)	HEK293T cells (CRL-3216) was purchased from ATCC. HEK293A cells (CRL-1573) was purchased from ATCC. Human Skeletal Muscle Cells (HSkMC, CP-H095, Pricella) was purchased from procell.
Authentication	No specific cell line authentication was performed.
Mycoplasma contamination	All cell lines were routinely tested for mycoplasma using a PCR detection kit (Sigma, MPO035). The results indicated that all cells were negative for mycoplasma.
Commonly misidentified lines (See ICLAC register)	None of the commonly misidentified lines were used in this study.

Animals and other research organisms

Policy information about studies involving animals; ARRIVE guidelines recommended for reporting animal research, and Sex and Gender in Research

Laboratory animals	cFeimin flox/flox was obtained from Viewsolid Biotech; Foxc2 flox/flox was obtained from GemPharmatech; HSA-Cre mice was obtained from MARC (Model Animal Research Center, Nanjing,PRC); C57BL/6J was obtained from GemPharmatech; AMPKa1&2 (Ampk) MKO mice and Ucp1-/- mice were previously reported. Studies were performed in 8-10 week old mice. Mice were housed in a temperature-controlled environment at around 21 °C with free access to food and water using a 12 hr light/12 hr dark cycle. All mice were maintained on a C57BL/6J background.
Wild animals	No wild animals were used in the study.
Reporting on sex	Both male and female mice were employed for this study.
Field-collected samples	No field-collected samples were used in the study.
Ethics oversight	Animals were maintained with all relevant ethical regulations for animal testing and research. All animal experiments were approved by the Animal Care and Use Committee at Tsinghua University.

Note that full information on the approval of the study protocol must also be provided in the manuscript.

Plants

Seed stocks	*Report on the source of all seed stocks or other plant material used. If applicable, state the seed stock centre and catalogue number. If plant specimens were collected from the field, describe the collection location, date and sampling procedures.*
Novel plant genotypes	*Describe the methods by which all novel plant genotypes were produced. This includes those generated by transgenic approaches, gene editing, chemical/radiation-based mutagenesis and hybridization. For transgenic lines, describe the transformation method, the number of independent lines analyzed and the generation upon which experiments were performed. For gene-edited lines, describe the editor used, the endogenous sequence targeted for editing, the targeting guide RNA sequence (if applicable) and how the editor was applied.*
Authentication	*Describe any authentication procedures for each seed stock used or novel genotype generated. Describe any experiments used to assess the effect of a mutation and, where applicable, how potential secondary effects (e.g. second site T-DNA insertions, mosiacism, off-target gene editing) were examined.*